Nuclear encoded photosynthesis genes are specifically controlled by the NuA4 complex

Tomasz Bieluszewski[1], Weronika Sura[1], Anna Bieluszewska[1], Michał Kabza[1], Mateusz Abram[1], Piotr Włodzimierz[1], Wojciech Dzięgielewski[1], Maja Szymańska-Lejman[1], Catherine Lachance[2], Nancy De Winne[3], Geert De Jaeger[3], Jacques Côté[2], Jan Sadowski[1], Piotr A. Ziolkowski[1]

[1] Laboratory of Genome Biology, Institute of Molecular Biology and Biotechnology, Adam Mickiewicz University, 61-614 Poznan, Poland

[2] Laval University Cancer Research Center, CHU de Québec-UL Research Center-Oncology Division, Quebec City, QC, G1R 3S3, Canada

[3] VIB-UGent Center for Plant Systems Biology, 9052 Ghent, Belgium

Correspondence: pzio@amu.edu.pl

Abstract

NuA4, an essential histone acetyltransferase complex, is required for efficient transcription in eukaryotes. Using genome editing, genomic approaches and biochemical assays, we characterized plant homologues of two key components of this complex, EPL1 and EAF1 in *Arabidopsis thaliana*. Surprisingly, we found that loss of AtEPL1, which is necessary for enzymatic activity of NuA4, is not lethal. Contrary to yeast, mutants lacking AtEAF1, responsible for complex targeting, display severe pleiotropic phenotype which copies that of *Atepl1*. *Atepl1* and *Ateaf1* mutants grow slowly, contain reduced chlorophyll levels and small chloroplasts. We provide evidence that these alterations are not caused by disturbance of GLK transcription factors, the major regulators of chloroplast development. Using ChIP-seq we show that H4 acetylation levels are dramatically reduced in the chromatin of the *Atepl1* mutant, while H3 acetylation remains mostly unchanged. We use our data to define NuA4-dependent genes and show that chloroplast-related genes are significantly overrepresented in this group, consistent with the pale-green phenotypes of the mutants. We propose that NuA4 was adopted in plants to control nuclear-encoded photosynthesis genes.

Keywords: EAF1 / EPL1 / H4 acetylation / NuA4 / photosynthesis

Significance

Photosynthesis depends on chloroplast proteins, most of which are nucleus-encoded and thus subject to control mechanisms common across eukaryotes. Here we show that NuA4, an evolutionary conserved transcriptional coactivator, is necessary for proper development of photosynthetic apparatus. Surprisingly, in contrast to yeast and metazoans, plants engineered to lack core NuA4 subunits are capable of vegetative development despite dramatic genome-wide loss of NuA4-dependent H4K5 acetylation. This chromatin perturbation seems to directly affect 350 genes which, in addition to reduced H4K5ac levels, display decreased transcript levels but no loss of transcription-related H3K9ac. A significant proportion of these genes are related to chloroplast function, particularly to translation, an intriguing parallel to the yeast NuA4's role in transcription of ribosome biogenesis-related genes.

Introduction

Substantial biochemical and genetic evidence support a functional interplay between chromatin structure and transcription in eukaryotes. The reverse genetic approach, possible due to advances made in yeast and animal models, provided a framework to our understanding of this relationship in plants. It is now evident that evolutionarily conserved enzymes and chromatin marks have been adopted in plants for functions in development, stress response and genome integrity. In fact, conserved chromatin transactions play central roles in regulation of plant-specific processes such as transition to flowering(1, 2) and flower morphogenesis(3, 4).

One of the characteristic features of plants are chloroplasts which carry out photosynthesis(5). As most of the chloroplast proteins are encoded by nuclear genes, chromatin should in principle have an influence on their expression. Molecular and genetic studies suggest that such a link may indeed exist in plants. Some observations showed that changes in the acetylation status of histones H3 and H4 over genes encoding plastidic proteins coincide with changes in light and nutrient availability as well as developmental stage(6, 7). Likewise, increased levels of H3K9 acetylation (H3K9ac) accompany increased transcriptional activity of these genes(8). In addition, mutations which disrupt genes involved in histone modifications and chromatin remodeling such as *AtGCN5*, *HAF2* (one of the two *Arabidopsis thaliana* genes encoding TAF1 homologues) or *BRM*, affect transcript levels of genes encoding plastidic proteins(9, 10). Interestingly, chromatin perturbations described so far produce mild photosynthetic or photomorphogenic phenotypes, despite often extreme impact on other processes(11). Here we show that the expression of the photosynthetic apparatus of a model plant *A. thaliana* depends on histone H4 acetylation by a highly conserved transcriptional coactivator, the Nucleosomal Acetyltransferase of H4 (NuA4) complex.

The budding yeast NuA4 complex consists of 13 different subunits which fall into 3 functional categories: enzyme, histone posttranslational modification reader and scaffold(12). Scaffold proteins Enhancer of Polycomb-Like 1 (EPL1), Esa1-Associated Factor 1 (EAF1) and Transcription-Associated 1 (TRA1) recruit reader subunits and transcription factors, greatly improving specificity of the acetyltransferase subunit Essential SAS2-related Acetyltransferase 1 (ESA1) towards histones H4, H2A and H2A.Z in the chromatin context(13–16). Molecular studies in yeast and animals support critical roles for the NuA4-dependent histone acetylation in DNA-repair and transcription(17, 18). Plant homologues of NuA4 subunits were linked by genetic studies to gametogenesis, ABA-responses, control of flowering time, chlorophyll synthesis, cell growth and ploidy(19–22). Some of these functions of the plant NuA4 have been confirmed to be mediated by acetylation of H4(21, 23, 24).

In this work, we introduce a set of genetic tools which gave us a unique opportunity to explore the consequences of complete loss of NuA4 integrity without compromising viability as in the case of the catalytic subunit mutants described in eukaryotic models before(19, 25, 26). Mutants lacking homologues of the scaffold subunits EPL1 or EAF1 consistently display pleiotropic phenotype, much more severe than the NuA4-mutant phenotypes described in plants so far. We show that the photosynthetic component of this phenotype is similar in magnitude, but different in origin, to the effects observed in the absence of the Golden2-Like (GLK) transcription factors which specifically promote chloroplast development in various plant species(27). Our genetic and transcriptomic analyses argue against NuA4 and GLKs acting in the same pathway. Instead, we show that loss of NuA4 integrity leads to dramatic global decrease of H4K5 acetylation with almost no impact on H3K9ac as well as widespread disruption of nuclear transcription. Our results suggest a direct link between NuA4 activity and expression of the GLK-independent nuclear genes encoding plastid ribosomal proteins(28) (npRPGs).

Results

NuA4 supports chloroplast development

The budding yeast NuA4 complex consists of two modules, the catalytic module called piccolo NuA4 (later picNuA4) and the regulatory module attached to picNuA4 through the platform subunit EAF1(12) (Fig. 1A). The EPL1 subunit plays a double role in NuA4 by enabling picNuA4 formation and binding to the regulatory part of the complex(15). Whereas the former function of EPL1 is essential, the latter is not(14). Consistently, the yeast strain lacking the C-terminal Enhancer of Polycomb B (EPcB) domain of EPL1 through which it binds to EAF1, phenocopies strains lacking functional EAF1(15). EAF1 and EPL1 are not only essential for the integrity of the NuA4 complex but also specific to NuA4, unlike most other subunits which

101 are shared with other protein complexes, therefore, they are key to understanding NuA4
102 function(15, 29). Despite growing interest in the plant NuA4 complex, little is known about plant
103 homologues of these two proteins.

104 Our previous study of Arabidopsis EAF1 (AtEAF1) could not reveal its full importance due to
105 the lack of a double mutant(24). Here, in order to generate a loss-of-function mutant, we
106 disrupted both *AtEAF1* genes simultaneously by Cas9-gRNA (Fig. 1B). During screening for
107 plants carrying heritable mutations, we observed the effects of sectorial somatic double knock-
108 out of *AtEAF1* which was manifested as green/pale green mosaicism (Fig. 1C). Microscopic
109 observation of the border regions between green and pale green sectors revealed a reduction
110 in the size of chloroplasts in the pale green (presumably EAF1-negative) sectors (Fig. 1C),
111 suggesting that AtEAF1 function is cell-autonomous. We observed the Cas9-gRNA induced
112 mosaicism in plants carrying all 3 independent Cas9-gRNA combinations although the
113 construct targeted downstream of the Swi3, Ada2, N-Cor and TFIIIB (SANT) domain produced
114 a weaker effect, suggesting a minor role of the C-terminal part of AtEAF1 in chloroplast
115 development (Fig. 1C). The association between the chloroplastic phenotype and the loss of
116 AtEAF1 was confirmed in the *Ateaf1-1* homozygous mutant which was evenly pale green (Fig.
117 1D). In this mutant line, the 11-kb deletion produced a chimeric *AtEAF1A/B* gene containing a
118 frameshift upstream of the SANT domain (Fig. 1B, Supplementary Fig. 1). The SANT domain
119 is vital to the function of yeast EAF1(15), therefore, we consider *Ateaf1-1* a loss-of-function
120 mutant and a reference for reverse genetics of the plant NuA4 complex.

121 *A. thaliana* contains two EPL1 orthologues which have been copurified with other plant NuA4
122 subunits previously(24, 30) but have not been studied genetically. In order to investigate the
123 function of AtEPL1, we generated a double T-DNA insertion mutant (later *Atepl1-1*) by crossing
124 two publicly available lines. Insertions in At1g16690 (*Atepl1a-1*) and At1g79020 (*Atepl1b-1*)
125 are located within EPcA (*Atepl1a-1*, Fig 1B) or between EPcA and EPcB domains (*Atepl1b-1*,
126 Fig. 1B). Whereas full-length transcripts are undetectable in the double homozygous mutant,
127 both loci still produce aberrant transcripts encoding a polypeptide homologous to the N-
128 terminal part of EPL1 (Fig. 1B), which is sufficient for picNuA4 activity in budding yeast but not
129 for the binding to the regulatory part of the complex(15) (Fig. 1A).

130 Since the yeast EPL1 serves two functions in the NuA4 complex, one of which is potentially
131 preserved in *Atepl1-1*, we used Cas9-gRNA to generate additional alleles of the *AtEPL1* genes.
132 In order to obtain null alleles, we introduced frame-shifting deletions in the 5' parts of the coding
133 regions of both genes (Fig. 1B, Supplementary Fig. 2 and 3). As lethal effect of a double
134 homozygous mutation was expected, we first generated two single homozygous mutants
135 (*Atepl1a-2* and *Atepl1b-2*) and crossed them to obtain the *Atepl1-2* double mutant. In addition,

136 we generated an in-frame deletion spanning the EPcB domain of AtEPL1B (*Atepl1b-3*, Fig. 1B,
137 Supplementary Fig. 3) and crossed the mutant to *Atepl1-2* to obtain the *Atepl1a-2 Atepl1b-3*
138 mutant (later referred to as *Atepl1-3*). Since the genomic deletion present in the *AtEPL1A* locus
139 in the *Atepl1-2* mutant starts in an exon and ends in an intron, the exact transcript sequence
140 cannot be predicted with confidence. In order to check if splicing of the *Atepl1a-2* allele leads
141 to a frameshift, we sequenced 6 independent cDNA clones derived from RNA isolated from a
142 homozygous *Atepl1-2* mutant. All clones displayed identical splicing pattern of the truncated
143 intron IV which led to a frameshift, therefore this allele is unlikely to produce even partially
144 functional AtEPL1A protein in significant amounts (Supplementary Fig. 2). Importantly, the
145 strong pleiotropic *Ateaf1*-like phenotype shared by the *Atepl1* homozygotes was fully rescued
146 in *Atepl1-1* homozygotes expressing tagged AtEPL1B (pAtEPL1B::AtEPL1B-TAP, Fig. 1D),
147 confirming loss of AtEPL1 as the cause of the phenotypic effects observed in *Atepl1* mutants.

148 **AtEPL1 is not essential for viability but key to NuA4 function**

149 Contrary to our predictions based on homology to yeast, where EPL1 is an essential gene, all
150 double *Atepl1* mutants described above were viable in double homozygote form, albeit clearly
151 more defective than other plant NuA4 subunit mutants characterized to date (Supplementary
152 Fig. 4). The viability of the *Atepl1* mutants gave us a unique opportunity to compare the relative
153 contributions made by the EAF1-dependent NuA4 holocomplex and EPL1-dependent picNuA4
154 in plants. We used four quantitative phenotyping assays to describe and compare the growth-
155 and photosynthesis-related phenotypes of *Ateaf1* and *Ateapl1* mutants. Additionally, we
156 included in our analyses the well-characterized *glk1-1 glk2-1* mutant (referred to as *glk* below)
157 in which cell-autonomous reduction in chloroplast size as well as significant reduction in rosette
158 diameter have been observed previously(27, 31).

159 As an approximation for chloroplast- and cell-size we used surface projection areas of the
160 organelles or cells obtained through live confocal imaging of the palisade mesophyll cell layer
161 of rosette leaves. In order to eliminate variability resulting from changes in chloroplast size
162 during leaf growth, we measured chloroplasts in fully expanded 4th leaves of 10-true-leaf-
163 rosettes. We found both chloroplasts and cells to be significantly smaller in all mutants
164 compared to wild type (WT) plants (Fig. 2A, Supplementary Table 1A). The NuA4 mutants
165 were indeed similar to the *glk* mutant in terms of chloroplast size but less so in terms of cell
166 size (Fig. 2A). Notably, the *Atepl1-2* null-mutant displayed stronger reduction in chloroplast
167 size than the *Ateaf1-1* mutant, possibly owing to residual non-targeted activity of picNuA4 in
168 this line. It remains unclear why *Atepl1-3* (picNuA4-separated) mutant is more phenotypically
169 similar to *Atepl1-2* than to *Ateaf1-1*.

170 Pale green coloration of the NuA4 and *glk* mutants indicates loss of chlorophyll. Indeed,
171 spectrophotometric analysis of chlorophyll content in 10-leaf rosettes showed significant
172 reduction of total chlorophyll in all mutants with the strongest effect in *glk*, followed by *Atepl1-*
173 *2*. The *Ateaf1-1* mutant again displayed the weakest effect (Fig 2B, Supplementary Table 1B).
174 Interestingly, the significant increase in the chlorophyll a / b ratio reported previously in *glk*(32)
175 does not occur in the NuA4 mutants (Fig. 2B, Supplementary Table 1B).

176 In order to characterize the vegetative growth phenotype of the mutants, we measured rosette
177 radius of soil-grown plants after 2, 3 and 4 weeks of growth in long day conditions. In this
178 assay, the *glk* mutant performed much better than the NuA4 mutants, suggesting that the
179 dwarfism of *Atepl1* and *Ateaf1* cannot be fully explained by chloroplast disfunction (Fig. 2C,
180 Supplementary Table 1C). All lines which contained mutations in NuA4 subunits showed
181 severely reduced size relative to WT plants in all time points (Fig. 2C, Supplementary Table
182 1C). Consistent with its relatively weak effect on cell size, *Ateaf1-1* mutation had significantly
183 smaller effect on growth than the *Atepl1-2* mutations (Fig. 2C, Supplementary Tables 1C).
184 Altogether, these results support a model in which AtEPL1 cooperates with AtEAF1 for most,
185 but not all, of its functionality as a picNuA4 subunit.

186 **NuA4 and GLKs have parallel roles in transcription**

187 The yeast NuA4 requires transcription factors for improved targeting to specific genomic
188 loci(13, 33). We hypothesized that the phenotypic similarity between the mutants of NuA4
189 subunits and GLK transcription factors was due to targeting of NuA4 by GLKs. To verify our
190 hypothesis, we generated a quadruple mutant *Atepl1a-2 Atepl1b-2 glk1-1 glk2-1* (later *Atepl1*
191 *glk*) by crossing *Atepl1-2* sesquimutant with the previously characterized *glk1-1 glk2-1*
192 homozygote(27). The quadruple homozygous mutant was viable but displayed significantly
193 aggravated phenotypic effects in all phenotypic assays (Fig 1, 2, Supplementary Table 1).
194 Notably, the increase in chlorophyll a / b ratio observed in the *glk* but not in the NuA4 mutants
195 was significantly dampened in the *Atepl1 glk* mutant (Fig. 2B, Supplementary Table 1B). These
196 results suggest that NuA4 and GLK have mostly independent functions in transcription of
197 genes related to growth and photosynthesis and may even have opposite effects on some
198 pathways.

199 Seeking explanation for the mutant phenotypes and genetic interactions described above, we
200 turned to transcriptome analysis. We analyzed RNA extracted from 10-true-leaf rosettes of
201 *Atepl1-1* and WT plants. Overall 5319 genes showed at least two-fold decrease (hypoactive
202 genes) or increase (hyperactive genes) of the steady-state transcript level in the mutant
203 (Supplementary Data 1). As expected, Gene Ontology analysis of the hypoactive group (2613
204 uniquely mapped IDs) revealed significant enrichment in genes associated with chloroplasts,

205 photosynthesis and growth (Fig. 3A, Supplementary Data 1). Hyperactive group (2654
206 uniquely mapped IDs) was significantly enriched in genes functionally related to plasma
207 membrane as well as responses to biotic and abiotic stimuli (Fig. 3A, 3B, Supplementary Data
208 1). Biotic stress marker genes were also induced in *Atepl1-1* seedlings, which practically rules
209 out a possibility of their activation by deteriorating external conditions over extended growth
210 periods (Supplementary Fig. 6). Subsequently, we compared our results with the publicly
211 available differential expression data for the 2-week-old *glk* mutant seedlings(34) accessed
212 through Gene Expression Omnibus (NCBI). In contrast to the *Atepl1-1* mutant, genes
213 differentially expressed in *glk* relative to WT control were predominantly hypoactive (866 vs 30
214 IDs, Fig. 3B). The small group of *glk*-hyperactive genes (30 IDs) showed negligible overlap
215 with the *Atepl1*-hyperactive gene group (Fig. 3B). The overlap between genes hypoactive in
216 *Atepl1-1* and *glk* was also relatively small (81 IDs). Surprisingly, genes hypoactive in *Atepl1-1*
217 showed much higher association with chloroplasts and photosynthesis than genes hypoactive
218 in *glk* (Fig. 3B). Finally, we used previously published transcriptomic data for inducible GLK-
219 overexpressor lines(32) to compare *Atepl1*-hypoactive genes with *glk*-hypoactive and GLK-
220 dependent genes (Fig. 3C). Upon closer examination of four manually curated groups of
221 functionally related genes, we found that both NuA4 and GLKs contribute to expression of
222 nuclear genes encoding proteins involved in chlorophyll biosynthesis and light harvesting,
223 whereas expression of nuclear plastid ribosomal protein genes (npRPGs) depends only on
224 NuA4 (Fig. 3C). This comparison shows that NuA4 has a much broader impact on expression
225 of photosynthesis-related genes than GLKs (Fig. 3C). Overall, these observations are in
226 agreement with our genetic analyses suggesting at least partially independent roles for NuA4
227 and GLKs in chloroplast development and maintenance.

228 **AtEPL1 is a subunit of the plant NuA4's catalytic module**

229 In order to further explore the molecular basis of the observed phenotypes of plant NuA4
230 mutants, we first had to test whether the physical interactions of AtEPL1 and AtEAF1 follow
231 predictions based on AA sequence homology to yeast proteins. In yeast, EPL1 interacts
232 directly with ESA1, the catalytic subunit of the complex. Arabidopsis MYST-family HATs,
233 HAM1 and HAM2, are widely accepted as ESA1 orthologs. We produced recombinant
234 AtEPL1A, AtEPL1B, HAM1 and HAM2 in bacteria and used two different *in vitro* methods to
235 test direct interactions between them. Firstly, we performed a pull-down experiment in which
236 HAM1 or HAM2 fused with His-tag were immobilized on a nickel resin and incubated with
237 AtEPL1A or AtEPL1B fused with GST-tag. Both EPL1 homologues were specifically pulled
238 down by both ESA1 homologues as no GST signal was detected in the eluate after His-GFP
239 was used as a bait or when no bait was used (Fig. 4A). As a second method, we employed
240 Far Western Blot (FWB) in which one of the recombinant proteins undergoes SDS-PAGE and

241 Western Blot. After renaturation, the bait protein attached to the PVDF membrane is incubated
242 with the potential interactor. Overlap between the bait and prey signal on the membrane after
243 immunodetection of the prey indicates an interaction. Through this approach we confirmed all
244 interactions detected by pull-down, which indicates that AtEPL1A and AtEPL1B interact
245 directly and interchangeably with HAM1 and HAM2 (Fig. 4B).

246 In yeast, the functional significance of the physical interaction between EPL1 and ESA1 lies in
247 the ability of picNuA4 (formed through binding of ESA1, YNG2 and EAF6 to EPL1) to acetylate
248 histones in the context of a nucleosome. In order to test if *A. thaliana* picNuA4 is capable of
249 nucleosomal histone acetylation, we co-expressed HAM1, AtEPL1A, ING2 and AtEAF6 in
250 bacteria and used the recombinant complex for in vitro acetylation assay (Fig. 4C, 4D).
251 Notably, using HAM1 as a bait for complex purification resulted in recovery of all recombinant
252 picNuA4 subunits which confirms that these four plant proteins interact physically to form a
253 complex homologous to yeast picNuA4 (Fig. 4C). The *in vitro* HAT assay confirmed the activity
254 of the Arabidopsis picNuA4 on native oligonucleosomes. As expected, tritium-labeled acetyl
255 groups were efficiently transferred to histones H2A and H4, with some preference for the latter,
256 when compared to the yeast complex (Fig. 4D). These results provide strong evidence for
257 evolutionary conservation of the subunit composition and the activity of the picNuA4 complex
258 between budding yeast and plants.

259 **AtEPL1 interacts with the subunits of the NuA4's regulatory module**

260 PicNuA4 interacts with the targeting module of the yeast NuA4 through the contact made by
261 the EPcB domain of EPL1 with EAF1. Our phenotypic analyses of the *Atepl1-3* and *Ateaf1-1*
262 mutants suggest that AtEAF1 and the EPcB domain of AtEPL1 are crucial elements of the
263 plant NuA4 complex. In order to find biochemical confirmation of this observation we performed
264 tandem affinity purification followed by mass spectrometry in which we used the *Atepl1-1*
265 mutant complemented with the *pAtEPL1B::AtEPL1B-TAP* construct. The experiment was
266 performed twice on hydroponically grown seedling. Notably, out of the 15 proteins specifically
267 copurified with AtEPL1B in both experiments, 12 were homologues of yeast NuA4 subunits,
268 including EAF1 and ESA1 (Table 1, Supplementary Data 2). This result confirms and improves
269 on previously published findings regarding potential protein interactors of AtEPL1B(30) and
270 other putative subunits of *A. thaliana* NuA4(22, 24, 30, 35) (summarized in Table 1). In
271 particular, the use of tandem affinity purification resulted in low total number of interactors but
272 high number of NuA4 subunit-homologues, indicating high specificity (Table 1, Supplementary
273 Data 2). In fact, our analysis identified only 5 proteins which show no homology to yeast NuA4
274 subunits as potential AtEPL1B interactors (Table 1, Supplementary Data 2). Two of these
275 proteins, AOG2 and BRD6, were copurified with *A. thaliana* NuA4 subunits previously, albeit

276 in much larger pools of additional interactors (Table 1)(24, 30, 36). Interestingly, the
277 uncharacterized bromodomain protein BRD6(37), previously copurified with SWC4(24) and
278 HAM1(30) (Table 1), is orthologous to BRD8, a subunit of the human equivalent of NuA4, the
279 TIP60/p400 complex, according to PANTHER Classification System(38, 39), indicating a
280 possible role as an accessory subunit of the plant NuA4. AOG2, on the other hand, may be of
281 interest in the context of the role of NuA4 in gametophyte development(36).

282 In order to test whether AtEPL1 interacts with the targeting part of NuA4 through direct binding
283 to AtEAF1, we performed pull-down assay in which a His-tagged fragment of AtEAF1B
284 corresponding to AAs 430-1322, His-HAM1 (positive control) or His-EGFP (negative control)
285 were used as baits and GST-AtEPL1B was used as prey. Only His-AtEAF1B and His-HAM1
286 were able to pull-down GST-EPL1B which confirmed a direct physical interaction between
287 AtEPL1B and AtEAF1B (Fig. 4E). These results support our homology-based model in which
288 AtEPL1 and AtEAF1 interact directly to provide a scaffold for the assembly of the plant NuA4
289 complex.

290 **Loss of AtEPL1 triggers genome-wide depletion of H4K5ac but not H3K9ac**

291 Despite global role of NuA4 in maintaining H4 acetylation, studies in yeast suggest stronger
292 NuA4-dependence in certain groups of genes such as genes related to ribosome
293 biogenesis(18, 40). We hypothesized that expression of some nuclear genome-encoded
294 chloroplast- and photosynthesis-related genes may depend on acetylation of H4K5 by plant
295 NuA4. Previous studies showed that expression of light-regulated genes in plants correlates
296 with and depends on local histone acetylation status, especially that of H3K9(8, 9). In order to
297 test our hypothesis, we profiled the NuA4-dependent H4K5ac and the GCN5/SAGA-dependent
298 H3K9ac genome-wide in the *Atepl1-2* mutant and WT plants. We expected some genes
299 hypoactive in the mutant to show reduced H3K9ac due to indirect effects such as retrograde
300 signaling. Conversely, preservation of H3K9ac coinciding with highly reduced H4K5ac and
301 transcript levels would point to direct NuA4-dependence.

302 We performed Chromatin Immunoprecipitation followed by DNA-sequencing (ChIP-seq) on 10
303 true-leaf rosettes of *Atepl1-2* and WT grown in the same conditions as plants used for RNA-
304 seq. In addition to H4K5ac and H3K9ac, we used antibodies specific to unmodified H3 for
305 normalization of the acetyl-mark signal to nucleosome occupancy. Due to expected global
306 changes in epitope abundance, we included a predetermined proportion of mouse chromatin
307 in our ChIPs as a reference ("spike-in").

308 As expected, NuA4 inactivation in the *Atepl1-2* mutant resulted in globally reduced levels of
309 H4K5ac mark. Its occupancy profiles, averaged across all expressed genes, show strong

310 reduction in the mutant throughout the 3000 bp region centered on TSS (Fig. 5A,
311 Supplementary Fig. 8). In contrast to H4K5ac, the profile of H3K9ac in *Atepl1-2* overlaps well
312 with WT, with only a slight increase within the peak downstream of TSS. Interestingly, the
313 averaged H3 occupancy in *Atepl1-2* showed a marked increase on both sides of TSS (Fig. 5A,
314 Supplementary Fig. 8).

315 As both acetyl marks are highly enriched downstream of TSS in the WT (Fig. 5A), we averaged
316 the signal over the first 500 bp of each transcribed region and used these values to make
317 comparisons between individual genes. While H3-normalized H4K5ac levels in *Atepl1-2*
318 showed strong and almost uniform reduction in this window, H3K9ac levels were preserved in
319 most genes, with few genes showing strong changes (Fig. 5B). In agreement with the role of
320 H3K9ac in transcriptional activation, we observed increased H3K9ac levels over strongly
321 *Atepl1*-hyperactive genes (Fig. 5C). On the other hand, despite strong H4K5ac reduction over
322 most genes, only some from them showed reduced transcript levels (Fig. 5C) suggesting that
323 NuA4-dependency is determined by additional locus-specific factors.

324 Expression of npRPGs specifically depends on H4 acetylation by NuA4

325 Due to synergistic action of NuA4 and SAGA over most genes in yeast(18), one plausible
326 explanation of decreased expression of some genes is a concomitant loss of both acetylation
327 marks in *Atepl1* mutants. In such cases, there is no basis for a direct link between their
328 expression and NuA4 activity. On the other hand, genes hypoactive in *Atepl1-2* showing no
329 significant reduction in H3K9ac but strong reduction in H4K5ac are potentially directly affected
330 by loss of H4K5ac. In order to strictly define this group of genes we set the following arbitrary
331 criteria: (i) Log_2 of transcript level fold change should be lower than -1.5, (ii) Log_2 of H4K5ac
332 fold change should be lower than -2, (iii) Log_2 of H3K9ac fold change should be higher than -
333 0.5 (Fig. 6A, Supplementary Data 3). We visualized distribution of all genes hypo- or
334 hyperactive in *Atepl1-1* across these three dimensions by plotting log_2-transformed fold change
335 values of the two acetyl-marks against each other, separately for hypo- and hyperactive genes.
336 (Fig. 6B). Notably, *Atepl1*-hyperactive genes are shifted towards the upper right corner of the
337 plot (increased H3K9ac, no reduction in H4K5ac), indicating a role for H3K9ac in their
338 increased activity in the mutant as well as some level of dependency of H4K5ac on H3K9ac or
339 transcription in *Atepl1* background. Distribution of the hypoactive genes is less skewed along
340 the Y-axis (i.e. roughly equal numbers of hypoactive genes gain and lose H3K9ac) which
341 suggests that their behavior is driven mostly by loss of H4K5ac. Application of the acetylation
342 fold change criteria (ii) and (iii) to *Atepl1*-hypoactive genes leaves 350 potentially NuA4-
343 dependent genes (Supplementary Data 3). Intriguingly, when tested against all *Atepl1*-
344 hypoactive genes, this set is significantly enriched in genes associated with growth and

345 photosynthesis (Fig. 6C, Supplementary Data 3). Nuclear genes encoding plastid ribosomal
346 proteins(28) deserve particular attention as nearly all of them cluster within or near the NuA4-
347 dependent sector (Fig. 6B, Supplementary Data 3). Furthermore, the median log_2 expression
348 FC of translation- and ribosome-related NuA4-dependent genes is significantly lower than that
349 of all hypoactive genes as could be expected from genes which directly depend on NuA4 for
350 efficient transcription (Fig. 6D). This suggests that NuA4 complex has been adopted to
351 specifically stimulate expression of growth and photosynthesis-related genes in plants.

352 Discussion

353 Our previous attempts at methodical genetic analysis of the plant NuA4 complex were hindered
354 by the tandem duplication of the gene encoding *A. thaliana* homologue of budding yeast
355 EAF1(24). The Cas9-induced loss of function mutant presented here brings new evidence
356 supporting a central role of AtEAF1 in the plant NuA4 (Fig. 1, 2). First of all, the phenotype of
357 the *Ateaf1-1* mutant is significantly more severe than the phenotypes of the *mrg*, *eaf7* and *yaf9*
358 mutants described previously(20, 22, 23). We note that lethal effects have been reported for
359 the *Atswc4* mutant as well as the double *ham* mutant(19, 41). These are probably not NuA4-
360 specific, however, due to AtSWC4's role in the SWR1 complex and potential NuA4-
361 independent roles of HAM in acetylation of non-histone substrates(41, 42). Furthermore, the
362 *Ateaf1-1* mutant displays an extreme enhancement of the photosynthetic and reproductive
363 phenotypes previously reported in the double mutant of AtYAF9, a confirmed interactor of
364 AtEAF1(22, 24).

365 In the absence of EAF1, picNuA4 remains capable of non-targeted nucleosomal histone
366 acetylation, enabling survival(14, 43). Deletion of the picNuA4-specific subunit EPL1/EPC1 is
367 lethal in yeast and in animals(44, 45). Our biochemical analyses of the two previously identified
368 *A. thaliana* homologues of EPL1(24, 46) link it unequivocally to the plant NuA4 complex and
369 acetylation of nucleosomal substrates (Fig. 4). Remarkably, we show that plants tolerate loss
370 of EPL1 despite dramatic genome-wide reduction of H4K5ac and severe disorganization of the
371 transcriptome (Fig. 1, 2, 3, 5). This unexpected result should be confronted with a recent study
372 showing that, in addition to the pair of EPL1 orthologues described herein, *A. thaliana* contains
373 two EPL1-related proteins (EPCR)(30). Despite marginal sequence similarity to EPL1, EPCRs
374 interact physically with HAM1 and HAM2(30), possibly explaining why essential functions of
375 HAMs and picNuA4 may be completed without AtEPL1. On the other hand, EPCRs do not
376 copurify with any other subunit of the plant NuA4(30) and the HAT activity of the EPCR-HAM
377 complex has not been proven yet, therefore, this explanation is only hypothetical.

378 Severe phenotype of *Ateaf1-1*, most probably caused by dissolution of the regulatory module
379 of NuA4, suggests that proper targeting of the picNuA4 activity is outstandingly important in

380 plants. To our knowledge, the phenotype of *Ateaf1-1* is not copied by any mutation disrupting
381 a nuclear transcription factor described to date in *A. thaliana*. Nevertheless, we found the cell-
382 autonomous photosynthetic phenotype shared by *Ateaf1* and *Atepl1* mutants to be reminiscent
383 of the well characterized double *glk* mutant (Fig. 2)(27, 31). We hypothesized that GLKs guide
384 NuA4 to genes related to chloroplast development and photosynthesis. Our genetic
385 experiments and transcriptomic analyses provide convincing evidence against this hypothesis.
386 Although *Ateaf1*, *Atepl1* and *glk* mutants display comparable levels of reduction in chloroplast
387 size and chlorophyll level, these phenotypes are enhanced in the quadruple *Atepl1 glk* mutant,
388 suggesting at least partial functional independence (Fig. 1, 2). While GLKs directly control
389 transcript levels of a relatively small set of genes, NuA4 influences a significant proportion of
390 all genes related to chloroplasts and photosynthesis with a particularly strong effect on GLK-
391 independent npRPGs (Fig. 3). Finally, GLKs were not copurified here with EPL1B nor with any
392 other NuA4 subunit used as a bait in the AP-MS experiments reported to date (Table 1). All
393 this implies that NuA4 and GLK operate mostly independently although a limited cooperation
394 in some loci cannot be excluded.

395 Since phenotypes of *Ateaf1* and *Atepl1* mutants differed quantitatively rather than qualitatively
396 (Fig. 1, 2), we assumed similarly widespread changes in H4K5ac occupancy in both cases.
397 Consequently, we focused on the *Atepl1-2* mutant which gave us a unique opportunity to
398 investigate the impact of complete NuA4 inactivation while at the same time providing hints to
399 explain the common phenotype. Interestingly, despite roughly equal numbers of hypo- and
400 hyper-active genes in *Atepl1*, the H4K5ac levels were globally decreased (Fig. 3, 5). This
401 suggests either synergistic control by various acetyl marks or no influence of H4K5ac on
402 transcription in most loci. Another important observation is the lack of a global negative
403 influence of H4K5ac reduction on H3K9ac levels. Such influence has been recently observed
404 in ESA1-depleted budding yeast(18). Furthermore, many of the *Atepl1*-hyperactive genes
405 became hyperacetylated on H3K9 in the mutant despite showing low acetylation levels in the
406 WT (Fig. 5, 6), suggesting that H3K9ac may effectively build up and stimulate transcription in
407 the absence of nucleosomal H4K5 acetylation in plants.

408 In yeast, certain groups of genes show high NuA4-dependence. These are mostly genes
409 involved in translation and other anabolic processes(18, 33, 40, 47, 48). Consistently, NuA4-
410 defficient yeast strains are hypersensitive to rapamycin which inhibits growth-promoting TOR
411 signaling(14). Our results suggest that in plants NuA4-dependence is shifted from cytoplasmic
412 to plastidic translation machinery. To the best of our knowledge none of chromatin factors
413 involved in transcription control characterized to date show similar photosynthetic-related
414 phenotypes while inactivated in plants. The nucleus-encoded plastid ribosomal protein genes
415 showed little loss of H3K9ac but strong and uniform reduction in H4K5ac and transcript levels,

416 indicating potential direct NuA4-dependence (Fig. 7). Since these and other nuclear genes
417 encoding chloroplastic proteins originated from a cyanobacterial endosymbiont, there is an
418 ongoing search for a mechanism which enabled their effective transfer to the nucleus. It has
419 been proposed that open chromatin configuration facilitates both acquisition and transcriptional
420 activity of new mitochondrial and chloroplastic insertions in the nuclear genome(49, 50). It is
421 not unlikely that further investigation of the mechanisms through which NuA4 affects chromatin
422 structure and transcription in plants will improve our understanding of the transition between
423 the endosymbiont and the chloroplast at the origin of the green lineage.

424 Materials and methods

425 Plant material

426 All *A. thaliana* mutants used in this work are in Col-0 background. T-DNA insertion mutants for
427 AtEPL1A (At1g16690, SAIL_239_D12(51), *Atepl1a-1*) and AtEPL1B (At1g79020,
428 SALK_094941(52), *Atepl1b-1*) were obtained from NASC and crossed to produce the double
429 mutant *Atepl1-1*. The previously characterized double homozygous transposon-insertion
430 mutant *glk1-1 glk2-1*(27) also comes from the NASC collection (NASC ID: N9807). All other
431 mutants were generated for this work through Cas9-gRNA mediated genome editing of WT
432 Col-0 plants and are described in detail in Supplementary Figures 1-3.

433 Mutant generation through Cas9-gRNA

434 **Preparation of genetic constructs.** The Cas9 expression cassette was created through
435 fusion of the *ICU2* promoter sequence cloned from genomic DNA following published
436 instructions(53) with the 3xFlag-NLS-hSpCas9-NLS::NosT cassette which was a gift from Dr
437 Jian-Kang Zhu(54). Following insertion of the Cas9 expression cassette into the pFGC vector
438 (a gift of Dr Jian-Feng Li(55)), the *Bam*HI site was moved from the 5'- to the 3'-end of the Nos
439 terminator. The *Bam*HI site was subsequently used for linearization of the plasmid and
440 insertion of gRNA cassettes by Gibson assembly-based cloning. The gRNA expression
441 cassette containing U6 promoter was a gift from Dr Jian-Kang Zhu(54). The U3 expression
442 cassette was created by replacing the U6 promoter with the *AtU3C* promoter cloned from
443 genomic DNA isolated from *A. thaliana* Ler ecotype following published sequence data(56).
444 The target sequences were found with CRISPR-P(57) (*Ateaf1-1*, *Atepl1-2*) or CRISPOR(58)
445 (*Atepl1-3*). Targeted mutagenesis of the gRNA expression cassettes was done by PCR-
446 amplification and recircularization of the pJET1.2-based gRNA vectors. The sequences of the
447 primers used for mutagenesis can be found in the Supplementary Table 3. **Editing strategy**
448 **and isolation of the mutants.** In order to generate genomic deletions within coding regions
449 of the target genes, double-gRNA-Cas9 constructs were integrated with the genome through

450 Agrobacterium mediated transformation(59). Transformed plants were selected on soil by
451 spraying with Basta (Bayer). Two primers flanking the expected deletion were used to identify
452 plants which accumulated somatic mutations apparent from the presence of short PCR
453 products corresponding to deletions between two neighboring cut sites. T2 plants were
454 screened for the absence of Cas9-gRNA T-DNA by PCR and genotyped again for the presence
455 of desired genomic deletions. Any mutations detected in this way were assumed heritable.
456 Subsequently PCR amplification products were cloned into pJET1.2 vector and plasmids
457 isolated from multiple single colonies were sequenced to determine the sequences of both
458 homologous loci. If plants were confirmed as frame-shift- (*Ateaf1-1*, *Atepl1-2*) or in-frame-
459 deletion mutants (*Atepl1-3*), they were backcrossed to Col-0 and propagated. Sequences of
460 all primers used for genotyping can be found in Supplementary Table 3.

461 **Phenotypic analyses**

462 For all phenotypic analyses plants were grown in peat pellets (Jiffy) in controlled conditions:
463 22°C, 80-90 µmol/(m^2s) PAR, 60% RH. In course of the growth rate analyses, plants were
464 imaged in one-week intervals with a stereomicroscope or a camera, depending on the size.
465 ImageJ software was used for image analyses to extract the distance between the tip of the
466 longest rosette leaf and rosette center(60).

467 For plastid- and cell-size measurements, leaves #4 were cut from 10-true-leaf rosettes,
468 vacuum-infiltrated with perfluoroperhydrophenanthrene(61), mounted on a slide and imaged
469 with the A1Rsi confocal microscope (Nikon). Z-stacks spanning the palisade mesophyll cell-
470 layer, acquired in transmitted-light and chlorophyll autofluorescence channels, were used for
471 analysis in ImageJ. Contours of cells and plastids were tracked manually and the surface area
472 of the resulting regions of interest (ROI) was treated as the surface projection area of the
473 measured structures. All calculations and statistical analysis was done using Microsoft Excel.

474 Chlorophyll was extracted from a single plant for each biological replicate. A 10-leaf rosette
475 was separated from the root, weighed and grinded in liquid nitrogen. After obtaining a fine
476 powder, 3 or 5 ml (depending on rosette size) of Tris-HCl-buffered 80% acetone was added
477 and grinding was continued until homogeneity. The thawed mixture was then transferred to a
478 10 ml glass tube wrapped in aluminum foil to prevent access of light, sealed and kept in 4°C
479 overnight. Directly before spectroscopic measurements 1.5 ml of the mixture was transferred
480 to 1.5 ml microtubes (Axygen) and centrifuged at 10,000 G for 5 min to pellet any debris. After
481 centrifugation the extract was transferred to a spectrophotometer cuvette and absorbance was
482 measured at 647 nm and 664 nm using BioSpectrometer kinetic (Eppendorf)
483 spectrophotometer against buffered acetone as blank. The number of samples processed in
484 parallel was limited to 4 in order to reduce the influence of the processing time on the

485 measurements. Total chlorophyll content as well as chlorophyll a / b ratio were calculated
486 according to published formulas(62) without correction for absorbance at 750 nm.

487 **Pull-down**

488 Recombinant proteins were expressed in *E. coli* strains BL21-CodonPlus-RP or Lemo21(DE3,
489 New England Biolabs). Bacterial lysates were prepared as previously described(48) with the
490 following modifications. GST-tag and His-tag fusion proteins were resuspended in PBS or
491 equilibration and wash buffer (50 mM sodium phosphate, pH 8.0, with 0.3 M sodium chloride,
492 10 mM imidazole) respectively, with addition of 1 mM phenylmethylsulfonyl fluoride (PMSF)
493 and cOmplete™ Mini EDTA-free Protease Inhibitor Cocktail (Roche). His-GFP or His-fusion
494 proteins were bound to HIS-Selec HF Nickel Affinity Gel (Sigma) for 1 hour, then washed and
495 incubated with recombinant GST-fusion proteins for additional 1 h at 4°C. The beads were
496 washed five times with wash buffer containing 0,5% NP40. The protein complexes were
497 analyzed by SDS/PAGE followed by WB analysis with anti-GST (B14; #sc-138; Santa Cruz)
498 and anti-His (#R940-25; Life Technology, Waltham, MA, USA) antibodies.

499 **Far Western Blotting**

500 This experiment was performed as previously described(63) with some modification. Briefly,
501 GST, GST-AtEPL1A and GST-AtEPL1B were purified on Glutathione Sepharose 4 Fast Flow
502 beads (GE Healthcare) for 1 h at 4°C. The beads were washed five times with PBS containing
503 1% Triton X-100. The GST-fusion proteins were eluted by heating at 95°C in SDS/PAGE
504 loading buffer, resolved by SDS/PAGE and transferred onto PVDF membrane. Proteins were
505 renatured by incubation of the membrane in AC buffer (20 mM Tris pH 7.5, 1 mM EDTA, 0.1
506 M NaCl, 10% glycerol, 0.1% Tween-20, 2% non-fat milk, 1 mM DTT) containing 6 M guanidine-
507 HCl for 30 min at RT. Subsequently, the membrane was washed with AC buffer containing 3
508 M guanidine-HCl for 30 min at RT. This step was followed by washing with AC buffer containing
509 0.1 M- and no-guanidine-HCl AC buffer at 4°C, for 30 min and overnight respectively. The
510 membrane was blocked for 8 h at 4 °C in 5% nonfat milk in the PBST buffer and subsequently
511 incubated with His-HAM1 or His-HAM2. Next, the membrane was washed with 5% nonfat milk
512 in the PBST buffer followed by three washes with PBST. To detect bait proteins bound to the
513 bait proteins (GST-fusions) on the membrane, standard immunodetection with anti-His
514 antibody (#R940-25; Life Technology, Waltham, MA, USA) was performed.

515 **In vitro acetylation assay**

516 **Genetic construct preparation.** Coding sequences of AtEPL1A, HAM1, ING2 and AtEAF6
517 were cloned to the pST44 polycistronic vector for protein expression in *E. coli*, according to the
518 original pST44 documentation(64). FLAG-tag was added to the N-terminus of AtEPL1A and

519 6xHis-tag was added to the C-terminus of HAM1. **Protein expression and purification.**
520 Protein expression was conducted in BL21(DE3)pLysS cells after 0.3 mM IPTG induction and
521 the complex was purified over Talon (Clontech) cobalt affinity resin as described previously(65)
522 via Ham1-6xHis, using 150 mM imidazole for elution. Presence of all subunits was visible on
523 Coomassie-stained SDS-PA gel and presence of HAM1-His and FLAG-AtEPL1A was
524 confirmed by Western blot. **HAT assays.** HAT assays were performed as described
525 previously(66) with some changes. Briefly, in liquid HAT assays 0.5 µg of purified human core
526 histones or native H1-depleted short oligonucleosomes were incubated together with
527 bacterially expressed plant picNuA4 (or yeast picNuA4 as a positive control) complexes with
528 ^{3}H-labeled acetyl-CoA (0.125 µCi) in HAT buffer (50 mM Tris-HCl pH 8.0, 50 mM [KCl+NaCl],
529 5% glycerol, 0.1 mM EDTA, 1 mM DTT, 1 mM PMSF, 10 mM sodium butyrate) at 30°C for 30
530 min. Subsequently, the reactions were spotted on P81 membrane (Whatman), which were then
531 air-dried, washed 3 times with 50 mM carbonate buffer pH 9.2, rinsed in acetone and after
532 soaking in scintillation cocktail used to count ^{3}H signal. Alternatively, reactions were resolved
533 by SDS-PAGE. After electrophoresis gel was stained in Coomassie to visualize proteins,
534 destained and incubated in EN3HANCE solution (Perkin Elmer). After washing and drying, gel
535 was incubated with film.

536 **Tandem Affinity Purification (TAP)**

537 The construct used for purification of proteins interacting with AtEPL1B was created by
538 replacing the Gateway cassette in pMDC99 vector with the *AtEPL1B* expression cassette. The
539 *AtEPL1B* cassette consisting of the genomic sequence of *AtEPL1B* (At1g79020) including 969
540 bp of the native upstream regulatory sequence, C-terminal GSrhino tag(67), native 3' UTR of
541 *AtEPL1B* and Nos terminator was assembled in the pMDC99 backbone through Gibson
542 assembly-based cloning. Growing of seedlings and TAP purifications using 50 g of six-day old
543 seedlings as input per experiment, were performed as described in (67). Bound proteins were
544 digested on-bead after a final wash with 500 µL 50 mM NH_4HCO_3 (pH 8.0). Beads were
545 incubated with 1 µg Trypsin/Lys-C in 50 µL 50 mM NH_4OH and incubated at 37°C overnight in
546 a thermomixer at 800 rpm. Next day, an extra 0.5 µg Trypsin/Lys-C was added and the digest
547 was further incubated for 2 hours at 37°C. Finally, the digest was separated from the beads
548 and centrifuged at 20800 rcf in an Eppendorf centrifuge for 5 min, the supernatant was
549 transferred to a new 1.5 mL Eppendorf tube. Peptides were purified on C18 Bond Elut OMIX
550 tips (Agilent) and purified peptides were dried in a Speedvac and stored at -20°C until MS
551 analysis. Co-purified proteins were identified by mass spectrometry using a Q Exactive mass
552 spectrometer (ThermoFisher Scientific) using standard procedures(68)). Proteins with at least
553 two matched high confident peptides were retained. Background proteins were filtered out
554 based on frequency of occurrence of the co-purified proteins in a large dataset containing 543

555 TAP experiments using 115 different baits(67). True interactors that might have been filtered
556 out because of their presence in the list of non-specific proteins were retained by means of
557 semi-quantitative analysis using the average normalized spectral abundance factors (NSAF)
558 of the identified proteins in the EPL1B TAPs. Proteins identified with at least two peptides in at
559 least two experiments, showing high (at least 10-fold) and significant [-log10(p-value(T-test))
560 ≥10] enrichment compared to calculated average NSAF values from a large dataset of TAP
561 experiments with non-related bait proteins, were retained(69).

562 **RNA-seq**

563 For RNA-seq WT and *Atepl1-1* plants were grown under LD conditions (16 h light and 8 h
564 darkness), under 80-90 μmol/(m^2s) of photosynthetically active radiation. Material was
565 collected at the developmental stage of ca. 10 leaves about 5 hours after light onset.

566 RNA for each biological repeat was extracted from 110 mg of rosette leaves number 5-6 (from
567 at least six plants) with TRI Reagent (Merck) and rounds of phenol-chloroform and chloroform
568 extractions followed by isopropanol precipitation. RNA was treated with RQ1 DNase I
569 (Promega), then extracted with phenol-chloroform and precipitated with ethanol. Pure RNA
570 solution was sent to Macrogen Europe (South Korea), where libraries and sequencing were
571 performed using Illumina chemistry. RNA-seq experiment was also validated by RT-qPCR
572 (Supplementary Fig. 5).

573 Adapters, poor quality regions (mean Phred quality < 5) and rRNA sequences were removed
574 from short reads using BBDuk2 program from BBTools suite (https://jgi.doe.gov/data-and-
575 tools/bbtools). Filtered reads shorter than 50 bp were excluded from the analysis. Expression
576 values for genes and transcripts (Araport11 annotations) were calculated using Salmon(70)
577 with sequence-specific bias and GC content bias correction. Differential expression analysis
578 on both gene and transcript level was performed using limma package(71) following a
579 previously published protocol(72). False discovery rate (FDR) threshold of 0.01 and fold
580 change threshold of $Log_2FC=1$ (Fig. 3) or $Log_2FC=1.5$ (Fig. 6) were used in the analyses.

581 **ChIP-seq**

582 ChIP-seq analysis was carried out on WT and *Atepl1-2* plants grown in the same conditions
583 as the plants used for RNA-seq and harvested at the same developmental stage. Chromatin
584 was isolated as previously described(73), enriched with 2% chromatin isolated from mouse
585 embryonic fibroblasts as spike-in control, and incubated with antibody (Abcam ab1791,
586 Millipore 07327, Millipore 07352) overnight at 4°C. Dynabeads Protein A (Thermo Fisher
587 Scientific) were added to the samples and incubated for another 2 hours at 4°C. The slurry
588 was washed twice with low salt buffer (with 150 mM NaCl), twice with high salt buffer (with 500

589 mM NaCl) and once with LiCl wash buffer (10 mM Tris-HCl, pH 8.0, 1 mM EDTA, 0.25 M LiCl,
590 1% Nonidet P-40, 0.5% sodium deoxycholate, 1 mM PMSF and protease inhibitor cocktail).
591 Chromatin was eluted through incubation in 1% SDS and 0.8 M NaHCO3 at 65°C and the
592 cross-links were reversed by overnight incubation at 65°C. Following Proteinase K treatment
593 and phenol/chloroform extraction, DNA was precipitated and DNA concentration was
594 measured with Qubit dsDNA HS Kit (Thermo Fisher Scientific). 10 ng (H3) or 2 ng (other
595 antibodies) of ChIP-ed DNA was used to prepare DNA libraries with MicroPlex Library
596 Preparation Kit v2 (Diagenode).

597 Adapters and poor-quality regions (mean Phred quality < 5) were removed from short reads
598 using BBDuk2 program from BBTools suite (https://jgi.doe.gov/data-and-tools/bbtools).
599 Filtered reads shorter than 35 bp were excluded from the analysis. Reads were then aligned
600 to the *A. thaliana* (TAIR10) and mouse (GRCm38) genomes using BWA-MEM aligner(74).
601 Sambamba(75) was used to process the aligned data and remove duplicated reads. Mapping
602 statistics, including the percentages of mapped reads and duplicates, were calculated
603 separately for *A. thaliana* genome (ChIP-Seq data) and mouse genome ("spike-in" data) using
604 BamTools(76). Normalized and smoothed coverage data used for ChIP-Seq plots was
605 calculated using DANPOS2(77) and corrected using the fraction of deduplicated "spike-in"
606 reads mapped to the mouse genome. Summary of ChIP-seq data is shown in Supplementary
607 Table 2.

608 **Statistical analysis and plotting tools**

609 All data was managed with Excel (Microsoft). All calculations and statistical tests not described
610 in RNA-seq or ChIP-seq sections were run and plotted in Excel, except Mann-Whitney U tests
611 run with an online calculator (http://www.statskingdom.com) and plots presented in Figures 2A
612 and 5B created with BoxPlotR(78) and R respectively (www.R-project.org). For creation of the
613 area proportional Venn diagrams presented in Figure 3B, the gene sets included in
614 Supplementary Data 1 were first analyzed for overlaps by BioVenn(79), then plotted with
615 Euler*APE*(80) and finally graphically adjusted (coloring, line formatting) in PowerPoint
616 (Microsoft). Gene set enrichment analyses presented in Figure 3 were performed with
617 PANTHER Overrepresentation Test(38, 39) (Supplementary Data 1). Gene set enrichment
618 analyses presented in Figure 6C were performed with DAVID Functional Annotation Tool(81,
619 82) (Supplementary Data 3).

620 ## Author Contributions

621 **Conceptualization:** TB, PAZ, JS

Experimental work: Preparation of mutant lines: TB, WS, AB, MA, PW, WD, MSz-L, Phenotypic analyses: TB, WD, MSz-L, RNA-seq/RT-qPCR: WS, TB, ChIP-seq/ChIP-qPCR: WS, TB, Protein-protein interactions: AB, TB, *In vitro* acetylation: WS, CL, AP-MS: NDW, TB

Data analysis: TB, MK, PAZ

Project administration: PAZ, JS

Supervision: PAZ, JC (*in vitro* acetylation only), GDJ (AP-MS only)

Writing and Editing: TB, PAZ with contributions from all authors

Acknowledgements

This work was supported by the Polish National Science Center (NCN) grants 2016/21/B/NZ2/01757 and 2016/22/E/NZ2/00455 to PAZ, 2015/17/N/NZ1/00028 to W.S. and the Foundation for Polish Science grant (POIR.04.04.00-00-5C0F/17-00) to PAZ. The PhD fellowship of T.B. was covered by the International PhD Programme of the Foundation for Polish Science (MPD/2010/3) and KNOW RNA Research Centre in Poznan (01/KNOW2/2014). Research in JC lab was supported by a Foundation grant from the Canadian Institutes of Health Research (FDN-143314). JC holds a Canada Research Chair in Chromatin Biology and Molecular Epigenetics. The four-month stay of WS in JC group was funded by NCN grant 2017/24/T/NZ1/00165.

References

1. R. Bastow, *et al.*, Vernalization requires epigenetic silencing of FLC by histone methylation. *Nature* **427**, 164–167 (2004).

2. R. B. Deal, C. N. Topp, E. C. McKinney, R. B. Meagher, Repression of flowering in Arabidopsis requires activation of FLOWERING LOCUS C expression by the histone variant H2A.Z. *Plant Cell* **19**, 74–83 (2007).

3. M. Calonje, R. Sanchez, L. Chen, Z. R. Sung, EMBRYONIC FLOWER1 participates in polycomb group-mediated AG gene silencing in Arabidopsis. *Plant Cell* **20**, 277–291 (2008).

4. M. Wu, *et al.*, SWI2/SNF2 chromatin remodeling ATPases overcome polycomb repression and control floral organ identity with the LEAFY and SEPALLATA3 transcription factors. *PNAS* **109**, 3576–3581 (2012).

5. P. Jarvis, E. López-Juez, Biogenesis and homeostasis of chloroplasts and other plastids. *Nat. Rev. Mol. Cell Biol.* **14**, 787–802 (2013).

6. Y. L. Chua, a P. Brown, J. C. Gray, Targeted histone acetylation and altered nuclease accessibility over short regions of the pea plastocyanin gene. *Plant Cell* **13**, 599–612 (2001).

7. S. Offermann, *et al.*, Developmental and environmental signals induce distinct histone acetylation profiles on distal and proximal promoter elements of the C4-Pepc gene in maize. *Genetics* **179**, 1891–901 (2008).

8. L. Guo, J. Zhou, A. A. Elling, J.-B. F. Charron, X. W. Deng, Histone modifications and

660 expression of light-regulated genes in Arabidopsis are cooperatively influenced by
661 changing light conditions. *Plant Physiol.* **147**, 2070–83 (2008).

662 9. M. Benhamed, C. Bertrand, C. Servet, D.-X. Zhou, Arabidopsis GCN5, HD1, and
663 TAF1/HAF2 interact to regulate histone acetylation required for light-responsive gene
664 expression. *Plant Cell* **18**, 2893–903 (2006).

665 10. D. Zhang, Y. Li, X. Zhang, P. Zha, R. Lin, The SWI2/SNF2 Chromatin-Remodeling
666 ATPase BRAHMA Regulates Chlorophyll Biosynthesis in Arabidopsis. *Mol. Plant* **10**,
667 155–167 (2016).

668 11. K. E. Vlachonasios, Disruption Mutations of ADA2b and GCN5 Transcriptional Adaptor
669 Genes Dramatically Affect Arabidopsis Growth, Development, and Gene Expression.
670 *Plant Cell* **15**, 626–638 (2003).

671 12. Y. Doyon, J. Côté, The highly conserved and multifunctional NuA4 HAT complex.
672 *Curr. Opin. Genet. Dev.* **14**, 147–154 (2004).

673 13. C. E. Brown, *et al.*, Recruitment of HAT Complexes by Direct Activator Interactions
674 with the ATM-Related Tra1 Subunit. *Science* **292**, 2333–2337 (2001).

675 14. A. A. Boudreault, *et al.*, Yeast Enhancer of Polycomb defines global Esa1-dependent
676 acetylation of chromatin. *Genes Dev.* **17**, 1415–1428 (2003).

677 15. A. Auger, *et al.*, Eaf1 is the platform for NuA4 molecular assembly that evolutionarily
678 links chromatin acetylation to ATP-dependent exchange of histone H2A variants. *Mol.*
679 *Cell. Biol.* **28**, 2257–70 (2008).

680 16. P. Xu, *et al.*, The NuA4 Core Complex Acetylates Nucleosomal Histone H4 through a
681 Double Recognition Mechanism. *Mol. Cell* **63**, 965–975 (2016).

682 17. X. Cheng, *et al.*, Phospho-dependent recruitment of the yeast NuA4 acetyltransferase
683 complex by MRX at DNA breaks regulates RPA dynamics during resection. *PNAS*
684 **115**, 10028–10033 (2018).

685 18. M. J. Bruzzone, S. Grünberg, S. Kubik, G. E. Zentner, D. Shore, Distinct patterns of
686 histone acetyltransferase and Mediator deployment at yeast protein-coding genes. **32**,
687 1252–1265 (2018).

688 19. D. Latrasse, *et al.*, The MYST histone acetyltransferases are essential for
689 gametophyte development in Arabidopsis. *BMC Plant Biol.* **8**, 121 (2008).

690 20. T. Umezawa, *et al.*, Genetics and phosphoproteomics reveal a protein phosphorylation
691 network in the abscisic acid signaling pathway in arabidopsis thaliana. *Sci. Signal.* **6**,
692 1–14 (2013).

693 21. V. Zacharaki, *et al.*, The Arabidopsis ortholog of the YEATS domain containing protein
694 YAF9a regulates flowering by controlling H4 acetylation levels at the FLC locus. *Plant*
695 *Sci.* **196**, 44–52 (2012).

696 22. P. Crevillén, *et al.*, Arabidopsis YAF9 histone readers modulate flowering time through
697 NuA4-complex-dependent H4 and H2A.Z histone acetylation at FLC chromatin. *New*
698 *Phytol.* **222**, 1893–1908 (2019).

699 23. Y. Xu, *et al.*, Arabidopsis MRG domain proteins bridge two histone modifications to
700 elevate expression of flowering genes. *Nucleic Acids Res.* **42**, 10960–74 (2014).

701 24. T. Bieluszewski, *et al.*, AtEAF1 is a potential platform protein for Arabidopsis NuA4
702 acetyltransferase complex. *BMC Plant Biol.* **15**, 1–15 (2015).

703 25. E. R. Smith, *et al.*, ESA1 is a histone acetyltransferase that is essential for growth in

704 yeast. *PNAS* **95**, 3561–5 (1998).

705 26. Y. Hu, *et al.*, Homozygous disruption of the tip60 gene causes early embryonic
706 lethality. *Dev. Dyn.* **238**, 2912–2921 (2009).

707 27. D. W. Fitter, D. J. Martin, M. J. Copley, R. W. Scotland, J. A. Langdale, GLK gene
708 pairs regulate chloroplast development in diverse plant species. *Plant J.* **31**, 713–727
709 (2002).

710 28. N. Tiller, R. Bock, The translational apparatus of plastids and its role in plant
711 development. *Mol. Plant* **7**, 1105–1120 (2014).

712 29. N. E. Searle, L. Pillus, Critical genomic regulation mediated by Enhancer of Polycomb.
713 *Curr. Genet.* **64**, 147–154 (2018).

714 30. L.-M. Tan, *et al.*, The PEAT protein complexes are required for histone deacetylation
715 and heterochromatin silencing. *EMBO J.* **37** (2018).

716 31. M. T. Waters, E. C. Moylan, J. A. Langdale, GLK transcription factors regulate
717 chloroplast development in a cell-autonomous manner. *Plant J.* **56**, 432–444 (2008).

718 32. M. T. Waters, *et al.*, GLK transcription factors coordinate expression of the
719 photosynthetic apparatus in Arabidopsis. *Plant Cell* **21**, 1109–1128 (2009).

720 33. J. L. Reid, V. R. Iyer, P. O. Brown, K. Struhl, Coordinate regulation of yeast ribosomal
721 protein genes is associated with targeted recruitment of Esa1 histone acetylase. *Mol.*
722 *Cell* **6**, 1297–1307 (2000).

723 34. Y. Nagatoshi, *et al.*, GOLDEN 2-LIKE transcription factors for chloroplast development
724 affect ozone tolerance through the regulation of stomatal movement. *PNAS* **113**,
725 4218–4223 (2016).

726 35. L. Vercruyssen, *et al.*, ANGUSTIFOLIA3 Binds to SWI/SNF Chromatin Remodeling
727 Complexes to Regulate Transcription during Arabidopsis Leaf Development. *Plant Cell*
728 **26**, 210–229 (2014).

729 36. L. A. Moody, *et al.*, A Musashi-Related Protein is Essential for Gametogenesis in
730 Arabidopsis. *bioRxiv* (2019) https:/doi.org/https://doi.org/10.1101/579714.

731 37. R. Pandey, *et al.*, Analysis of histone acetyltransferase and histone deacetylase
732 families of Arabidopsis thaliana suggests functional diversification of chromatin
733 modification among multicellular eukaryotes. *Nucleic Acids Res.* **30**, 5036–5055
734 (2002).

735 38. H. Mi, A. Muruganujan, D. Ebert, X. Huang, P. D. Thomas, PANTHER version 14:
736 More genomes, a new PANTHER GO-slim and improvements in enrichment analysis
737 tools. *Nucleic Acids Res.* **47**, D419–D426 (2019).

738 39. H. Mi, *et al.*, Protocol Update for large-scale genome and gene function analysis with
739 the PANTHER classification system (v.14.0). *Nat. Protoc.* **14**, 703–721 (2019).

740 40. D. Rossetto, *et al.*, Eaf5/7/3 form a functionally independent NuA4 submodule linked
741 to RNA polymerase II-coupled nucleosome recycling. *EMBO J.* **33**, 1397–415 (2014).

742 41. Á. Gómez-Zambrano, *et al.*, Arabidopsis SWC4 Binds DNA and Recruits the SWR1
743 Complex to Modulate Histone H2A.Z Deposition at Key Regulatory Genes. *Mol. Plant*
744 **11**, 815–832 (2018).

745 42. Z. Du, *et al.*, DNMT1 Stability Is Regulated by Proteins Coordinating Deubiquitination
746 and Acetylation-Driven Ubiquitination. *Sci. Signal.* **3**, ra80 (2010).

747 43. D. S. Ginsburg, C. K. Govind, A. G. Hinnebusch, NuA4 Lysine Acetyltransferase Esa1
748 Is Targeted to Coding Regions and Stimulates Transcription Elongation with Gcn5.
749 *Mol. Cell. Biol.* **29**, 6473–6487 (2009).

750 44. L. Galarneau, *et al.*, Multiple links between the NuA4 histone acetyltransferase
751 complex and epigenetic control of transcription. *Mol. Cell* **5**, 927–937 (2000).

752 45. T. Sato, M. A. Russell, R. E. Denell, Homoeosis in Drosophila: a new enhancer of
753 polycomb and related homoeotic mutations. *Genetics* **105**, 357–70 (1983).

754 46. N. M. Springer, *et al.*, Sequence relationships, conserved domains, and expression
755 patterns for maize homologs of the polycomb group genes E(z), esc, and E(Pc). *Plant*
756 *Physiol* **128**, 1332–1345 (2002).

757 47. X. Cheng, *et al.*, Eaf1 Links the NuA4 Histone Acetyltransferase Complex to Htz1
758 Incorporation and Regulation of Purine Biosynthesis. *Eukaryot. Cell* **14**, 535–544
759 (2015).

760 48. A.-L. Steunou, *et al.*, ComSteunou, A.-L., Cramet, M., Rossetto, D., Aristizabal, M.J.,
761 Lacoste, N., Drouin, S., Côté, V., Paquet, E., Utley, R.T., Krogan, N., et al. (2016).
762 Combined Action of Histone Reader Modules Regulates NuA4 Local Acetyltransferase
763 Function but Not Its Re. *Mol. Cell. Biol.* **36**, 2768–2781 (2016).

764 49. J. Tsuji, M. C. Frith, K. Tomii, P. Horton, Mammalian NUMT insertion is non-random.
765 *Nucleic Acids Res.* **40**, 9073–9088 (2012).

766 50. D. Wang, J. N. Timmis, Cytoplasmic organelle DNA preferentially inserts into open
767 chromatin. *Genome Biol. Evol.* **5**, 1060–1064 (2013).

768 51. A. Sessions, *et al.*, A high-throughput Arabidopsis reverse genetics system. *Plant Cell*
769 **14**, 2985–2994 (2002).

770 52. J. M. Alonso, *et al.*, Genome-Wide Insertional Mutagenesis of Arabidopsis thaliana.
771 *Science* **301**, 653–657 (2003).

772 53. Y. Hyun, *et al.*, Site-directed mutagenesis in Arabidopsis thaliana using dividing tissue-
773 targeted RGEN of the CRISPR/Cas system to generate heritable null alleles. *Planta*
774 **241**, 271–284 (2014).

775 54. Z. Feng, *et al.*, Multigeneration analysis reveals the inheritance, specificity, and
776 patterns of CRISPR/Cas-induced gene modifications in Arabidopsis. *PNAS* **111**,
777 4632–4637 (2014).

778 55. J.-F. Li, *et al.*, Multiplex and homologous recombination–mediated genome editing in
779 Arabidopsis and Nicotiana benthamiana using guide RNA and Cas9. *Nat. Biotechnol.*
780 **31**, 688–691 (2013).

781 56. C. Marshallsay, T. Kiss, W. Filipowicz, Amplification of plant U3 and U6 snRNA gene
782 sequences using primers specific for an upstream promoter element and conserved
783 intragenic regions. *Nucleic Acids Res.* **18**, 3459–3466 (1990).

784 57. Y. Lei, *et al.*, CRISPR-P: A Web Tool for Synthetic Single-Guide RNA Design of
785 CRISPR-System in Plants. *Mol. Plant* **7**, 1494–1496 (2014).

786 58. M. Haeussler, *et al.*, Evaluation of off-target and on-target scoring algorithms and
787 integration into the guide RNA selection tool CRISPOR. *Genome Biol.* **17**, 1–12
788 (2016).

789 59. S. J. Clough, A. F. Bent, Floral dip: a simplified method forAgrobacterium-mediated
790 transformation ofArabidopsis thaliana. *Plant J.* **16**, 735–743 (1998).

791 60. C. T. Rueden, *et al.*, ImageJ2: ImageJ for the next generation of scientific image data.
792 *BMC Bioinformatics* **18**, 529 (2017).

793 61. G. R. Littlejohn, *et al.*, An update: improvements in imaging perfluorocarbon-mounted
794 plant leaves with implications for studies of plant pathology, physiology, development
795 and cell biology. *Front. Plant Sci.* **5**, 140 (2014).

796 62. R. J. Porra, W. A. Thompson, P. E. Kriedemann, Determination of accurate extinction
797 coefficients and simultaneous equations for assaying chlorophylls a and b extracted
798 with four different solvents: verification of the concentration of chlorophyll standards by
799 atomic absorption spectroscopy. *BBA - Bioenerg.* **975**, 384–394 (1989).

800 63. A. Bieluszewska, M. Weglewska, T. Bieluszewski, K. Lesniewicz, E. Poreba, PKA-
801 binding domain of AKAP8 is essential for direct interaction with DPY30 protein. *FEBS*
802 *J.* **285**, 947–964 (2018).

803 64. S. Tan, R. C. Kern, W. Selleck, The pST44 polycistronic expression system for
804 producing protein complexes in Escherichia coli. *Protein Expr. Purif.* **40**, 385–395
805 (2005).

806 65. W. Selleck, I. Fortin, D. Sermwittayawong, J. Côté, S. Tan, The Saccharomyces
807 cerevisiae Piccolo NuA4 histone acetyltransferase complex requires the Enhancer of
808 Polycomb A domain and chromodomain to acetylate nucleosomes. *Mol. Cell. Biol.* **25**,
809 5535–42 (2005).

810 66. P. A. Grant, *et al.*, Yeast Gcn5 functions in two multisubunit complexes to acetylate
811 nucleosomal histones: Characterization of an ada complex and the saga (spt/ada)
812 complex. *Genes Dev.* **11**, 1640–1650 (1997).

813 67. J. Van Leene, *et al.*, An improved toolbox to unravel the plant cellular machinery by
814 tandem affinity purification of Arabidopsis protein complexes. *Nat Protoc* **10**, 169–187
815 (2015).

816 68. H. Nelissen, *et al.*, Dynamic changes in ANGUSTIFOLIA3 complex composition reveal
817 a growth regulatory mechanism in the maize leaf. *Plant Cell* **27**, 1605–1619 (2015).

818 69. J. Van Leene, *et al.*, Capturing the phosphorylation and protein interaction landscape
819 of the plant TOR kinase. *Nat. Plants* **5**, 316–327 (2019).

820 70. R. Patro, G. Duggal, M. I. Love, R. A. Irizarry, C. Kingsford, Salmon provides fast and
821 bias-aware quantification of transcript expression. *Nat. Methods* **14**, 417–419 (2017).

822 71. M. E. Ritchie, *et al.*, Limma powers differential expression analyses for RNA-
823 sequencing and microarray studies. *Nucleic Acids Res.* **43**, e47 (2015).

824 72. C. W. Law, M. Alhamdoosh, S. Su, G. K. Smyth, M. E. Ritchie, RNA-seq analysis is
825 easy as 1-2-3 with limma, Glimma and edgeR [version 1; referees: 3 approved].
826 *F1000Research* **5**, 1–29 (2016).

827 73. W. Sura, *et al.*, Dual Role of the Histone Variant H2A.Z in Transcriptional Regulation
828 of Stress-Response Genes. *Plant Cell Online* **29** (2017).

829 74. H. Li, Aligning sequence reads, clone sequences and assembly contigs with BWA-
830 MEM. **00**, 1–3 (2013).

831 75. A. Tarasov, A. J. Vilella, E. Cuppen, I. J. Nijman, P. Prins, Sambamba: Fast
832 processing of NGS alignment formats. *Bioinformatics* **31**, 2032–2034 (2015).

833 76. D. W. Barnett, E. K. Garrison, A. R. Quinlan, M. P. Stŕmberg, G. T. Marth, Bamtools: A
834 C++ API and toolkit for analyzing and managing BAM files. *Bioinformatics* **27**, 1691–
835 1692 (2011).

836 77. K. Chen, *et al.*, DANPOS: Dynamic analysis of nucleosome position and occupancy by
837 sequencing. *Genome Res.* **23**, 341–351 (2013).

838 78. M. Spitzer, J. Wildenhain, J. Rappsilber, M. Tyers, BoxPlotR: A web tool for generation
839 of box plots. *Nat. Methods* **11**, 121–122 (2014).

840 79. T. Hulsen, J. de Vlieg, W. Alkema, BioVenn - A web application for the comparison
841 and visualization of biological lists using area-proportional Venn diagrams. *BMC*
842 *Genomics* **9**, 1–6 (2008).

843 80. L. Micallef, P. Rodgers, euler APE: Drawing area-proportional 3-Venn diagrams using
844 ellipses. *PLoS One* **9** (2014).

845 81. D. W. Huang, B. T. Sherman, R. A. Lempicki, Systematic and integrative analysis of
846 large gene lists using DAVID bioinformatics resources. *Nat. Protoc.* **4**, 44–57 (2009).

847 82. D. W. Huang, B. T. Sherman, R. A. Lempicki, Bioinformatics enrichment tools: Paths
848 toward the comprehensive functional analysis of large gene lists. *Nucleic Acids Res.*
849 **37**, 1–13 (2009).

850 Main figure legends

851 **Figure 1. *Ateaf1* and *Atepl1* mutants as tools for genetic dissection of the plant NuA4**
852 **complex. A**, Schematic overview of the NuA4 complex engaging chromatin. The catalytic
853 module picNuA4 and the regulatory module are colored orange and blue, respectively. The
854 asterisk between EAF7 and ARP4 indicates the lack of an EAF5 homologue in plants.
855 Approximate positions of the crucial protein domains are indicated by the labels outside the
856 shapes representing the subunits. **B**, Gene structure diagrams of the *AtEAF1* and *AtEPL1* loci.
857 Target sites for the three double-gRNA constructs (gRNA pairs) used for *AtEAF1* mutagenesis
858 are depicted by arrows. Shaded areas delimit Cas9-gRNA-induced deletions (Δ) characterizing
859 particular alleles. Grey arrowheads indicate T-DNA insertion sites. Small black arrowheads
860 represent primers used for the RT-PCR presented in the panel on the right. **C**, Transgenic
861 plants carrying the three different Cas9-gRNA constructs. The scale bar length is 10 mm in all
862 images. Lower panels are confocal images of chlorophyll autofluorescence in the palisade
863 mesophyll cell layer of a leaf, centered on the border regions between green (upper part) and
864 pale green (lower part) sectors. Red outlines delimit selected cells and chloroplasts. The scale
865 bar is 50 µm in all micrographs. **D**, 4-week-old WT and mutant plants grown in the same
866 conditions. The insets show 4x magnifications of the same image.

867 **Figure 2. Phenotypic analysis of the NuA4 and GLK mutant lines. A**, Quantification of the
868 chloroplast- and cell-size data acquired by microscopic imaging of the palisade mesophyll cell
869 layer. Each circle represents a median surface area of 20 chloroplasts or 9 cells measured in
870 a single biological replicate (a single confocal stack from a separate plant). Statistical
871 significance was determined by two-tailed Mann-Whitney U test. The chlorophyll
872 autofluorescence images below the plots are projections of example stacks used for the

873 measurements. All images are in the same scale. The length of the scale bar is 50 µm. **B**,
874 Determination of total chlorophyll content and chlorophyll a / b ratio by spectroscopic analysis
875 of extracted chlorophyll. Dots represent means of 3 biological replicates. The whiskers delimit
876 95% confidence intervals. Statistical significance was determined by two-tailed t test. **C**,
877 Quantification of the growth phenotype of the mutants. The nodes represent the mean rosette
878 radius of 10 or 20 (*Atepl1-2*) plants grown in parallel. The whiskers delimit 95% confidence
879 intervals. P values are given for *Atea1-1* vs *Atepl1-2* (upper) and *Atepl1-2* vs *Atepl1 glk* (lower)
880 comparisons. Statistical significance was determined by two-tailed t test.

881 **Figure 3. Transcriptomic analysis of the NuA4 and GLK mutants. A**, Gene ontology
882 enrichment analysis of the *Atepl1-1* hypo- and hyperactive genes. Five representative GO
883 categories displayed in each graph were selected manually from the lists presented in
884 Supplementary Data 1. Gene enrichment analyses were performed using PANTHER
885 Overrepresentation Test (Supplementary Data 1). **B**, Area proportional Venn diagrams
886 illustrating overlaps between genes exhibiting the same direction of expression change in
887 *Atepl1-1* and *glk1* mutants as well as the gene sets representing particular GO categories. All
888 numerical values indicate numbers of genes present in a single sector of the diagram rather
889 than total values for sets. **C**, Relative transcript levels of genes encoding four selected groups
890 of chloroplast proteins in *Atepl1-1*, *glk*, *GLK1ox* (*G1*) and *GLK2ox* (*G2*) lines. Expression data
891 for the *glk* mutant and *GLKox* lines come from published works. Grey fields indicate no
892 significant change.

893 **Figure 4. Biochemical characterization of the plant picNuA4. A**, Pull-down assay showing
894 interaction between recombinant AtEPL1 and HAM paralogue pairs expressed in bacteria.
895 Pull-down and Input are abbreviated as P-D and INP, respectively. **B**, Interactions between
896 AtEPL1s and HAMs tested by Far Western Blot approach. After SDS-PAGE and Western Blot
897 of free GST and GST-AtEPL1A/B, the upper membranes were sequentially incubated with
898 HisHAM1/2 and anti-His antibody whereas the lower membranes were incubated with anti-
899 GST antibody. The lower bands in the upper panels most probably indicate HAM1/2 interaction
900 with partially degraded AtEPL1B. **C**, Purification of the recombinant *A. thaliana* picNuA4 from
901 bacteria (left panel, Coomassie staining). 6xHis-tag fused to HAM1 was used for purification
902 on cobalt affinity resin. Numbers in brackets indicate expected molecular weights of the
903 recombinant picNuA4 subunits. **D**, In vitro test of HAT activity of the recombinant *A. thaliana*
904 (*At*) picNuA4 towards short oligonucleosomes (SON). Recombinant *S. cerevisiae* (*Sc*)
905 picNuA4 was used as a positive control. Autoacetylation on AtEAF6 is highlighted by an
906 asterisk. **E**, Pull-down assay showing the interaction between AtEPL1B and a fragment of
907 AtEAF1B corresponding to AA 430-1322. HAM1 is used for comparison. All proteins were
908 expressed in bacteria as either GST- or 6xHis-fusions.

909 **Figure 5. Chromatin landscape of the *Atepl1-2* mutant. A**, TSS-centered profiles of spike-
910 in-normalized occupancy of H3, H3K9ac or H4K5ac averaged over all genes expressed in WT
911 Col-0. Vertical axes values are relative. Horizontal axes values represent chromosomal
912 position relative to TSS (i.e. negative values represent promoter region whereas positive
913 values represent gene body). **B**, Scatter plots showing differences in H3, H3K9ac or H4K5ac
914 occupancy between *Atepl1-2* and WT. Each dot represents Log_2-transformed ChIP-seq signal
915 averaged over the first 500 bp downstream from TSS of a single gene in WT and in *Atepl1-2*.
916 The number of dots per pixel is color-coded. **C**, A fragment of chromosome 4 showing spike-
917 in-normalized H3, H3K9ac or H4K5ac occupancy across several loci. The particular
918 chromosomal location was chosen to illustrate chromatin environment changes coinciding with
919 increased (orange gene) or decreased (blue) transcript levels versus no significant change
920 (white). Vertical axes values are relative.

921 **Figure 6. Identification of the potentially NuA4-dependent genes. A**, Ideogram of the
922 NuA4-dependency determination process. **B**, Scatter plot showing relationships between Log_2-
923 transformed fold-change of the spike-in- and H3-normalized H3K9ac and H4K5ac occupancy
924 and the directionality of the transcript level change. The dashed line delimits the ”NuA4-
925 dependent” area of the plot as described in (A). **C**, Functional enrichment and relative
926 expression of NuA4-dependent genes. P value for functional enrichment (column 5) is
927 equivalent to EASE score (modified Fisher Exact test, see Methods). P values for the
928 differences between median fold change against all genes hypoactive in *Atepl1-1* (column 8)
929 are results of Mann Whitney U test. GT stands for GO Term.

930 Supplementary figure legends

931 **Supplementary Figure 1. DNA sequence analysis of the *Ateaf1-1* allele. A**, Gene structure
932 diagram of the *AtEAF1* loci. Two different sequences targeted by gRNAs from the same
933 genetic construct (#2) are marked with red and purple. Due to almost identical sequence of the
934 two *AtEAF1* genes, each gRNA targeted both genes resulting in the total of four cut sites on
935 each chromosome. **B**, A representative sequencing result of a genomic PCR clone from a
936 single homozygous plant aligned with a fragment of the reference genomic sequences of
937 *AtEAF1A and AtEAF1B.* All sequence alignment images in Supplementary Figures 1-3 were
938 generated with Geneious 10 (Biomatters).

939 **Supplementary Figure 2. DNA sequence analysis of the *Atepl1a-2* allele. A**, Gene
940 structure diagram of the *AtEPL1A* locus. Two different sequences targeted by gRNAs from the
941 same genetic construct are marked with red and purple. **B**, A representative sequencing result
942 of a genomic PCR clone from a single homozygous plant aligned with a fragment of the

943 reference genomic sequence of *AtEPL1A.* The deletion starts in the exon II and ends in the
944 intron IV (downstream from the second cut site), therefore, the protein product cannot be
945 predicted based on the genomic sequence. The target sequences are framed and color-coded.
946 Black arrow heads mark Cas9-gRNA cut sites. **C**, Sequences of 6 independent cDNA clones
947 from a single homozygous mutant plant aligned with a fragment of the reference sequence of
948 the *AtEPL1A* CDS. CDNA sequencing suggests that all transcripts are spliced in the same way
949 which results in early translation termination. All sequence alignment images in Supplementary
950 Figures 1-3 were generated with Geneious 10 (Biomatters).

951 **Supplementary Figure 3. DNA sequence analysis of the *Atepl1b-2* and *-3* alleles. A**, Gene
952 structure diagram of the *AtEPL1B* locus. Two different sequences targeted by gRNAs from
953 each of the two genetic constructs are marked with red and purple (*Atepl1b-2*) or orange and
954 cyan (*Atepl1b-3*). **B**, A representative sequencing result of a genomic PCR clone from a single
955 *Atepl1b-2* homozygous plant aligned with a fragment of the reference genomic sequence of
956 *AtEPL1B.* The target sequences are framed and color-coded. Black arrow heads mark Cas9-
957 gRNA cut sites. **C**, A representative sequencing result of a genomic PCR clone from a single
958 *Atepl1b-3* homozygous plant aligned with a fragment of the reference genomic sequence of
959 *AtEPL1B.* All sequence alignment images in Supplementary Figures 1-3 were generated with
960 Geneious 10 (Biomatters).

961 **Supplementary Figure 4. The phenotype of *Atepl1-1* is more severe than the *Atyaf9a-1*
962 *Atyaf9b-2* mutant phenotype. A,** Quantitative description of 8-true leaf rosettes. Plants were
963 grown on peat pellets (Jiffy) in the following conditions: 22°C, 16-hour light period, 40
964 µmol/(m^2s) PAR, 70%. Error bars represent standard deviation. **B**, RT-qPCR analysis of
965 relative gene expression in whole rosettes grown and collected as described above. Error bars
966 represent standard deviation. Asterisks indicate significant differences relative to WT (two-
967 tailed t-test, $p < 0.05$). **C**, Main stems of representative WT and *Atepl1-1* plants grown in the
968 same conditions. **D**, Mean seed number per silique for siliques 11-20 collected from the main
969 stem from three plants for each line. Error bars represent standard deviation.

970 **Supplementary Figure 5. Validation of the RNA-seq data by RT-qPCR.** Relative transcript
971 levels of selected genes encoding proteins involved in chlorophyll biosynthesis were measured
972 by RT-qPCR. Error bars represent standard deviation of the sample (3 biological replicates).
973 The WT and *Atepl1-1* plants used for RNA extraction were grown in the same conditions as
974 plants for RNA-seq (see Methods). If no significant difference between WT and *Atepl1-1* was
975 detected by RNA-seq the data is not plotted (indicated by a black dot).

976 **Supplementary Figure 6. Early onset of the pathogen response-like transcriptomic
977 pattern in *Atepl1-1*. A**, Representative images of plant material collected for the RT-qPCR

978 analysis. Approximately 30 seedlings were used for each of the three biological replicates. **B**,
979 RT-qPCR analysis of relative gene expression in 2-true leaf seedlings compared with RNA-
980 seq data for 10-leaf rosettes obtained as described in Methods. Plants for RT-qPCR were
981 grown on peat pellets (Jiffy) in the following conditions: 22°C, 16-hour light period, 40
982 µmol/(m^2s) PAR, 70% RH. Error bars represent standard deviation.

983 **Supplementary Figure 7. ChIP-qPCR survey of chromatin perturbations in *Atepl1-2* and**
984 ***Ateaf1-1* mutants.** Two *Atepl1*-hypoactive genes (*QQS*, *CHLI1*), one *Atepl1*-hyperactive
985 stress-inducible gene (*PR1*) and one silent transposon (*Ta3*) were used to check for effects of
986 *Atepl1* and *Ateaf1* mutations on chromatin. The graphs represent data for a single biological
987 sample for each line. The error bars represent standard deviation of 3 technical replicates.

988 **Supplementary Figure 8. TSS ChIP-seq plots. A**, TSS-centered profiles of spike-in-
989 normalized occupancy of H3, H3K9ac or H4K5ac averaged over all genes expressed in WT
990 Col-0 (the same as in Fig. 5A), *Atepl1*-hypoactive or *Atepl1*-hyperactive genes. Vertical axes
991 values are relative. Horizontal axes values represent chromosomal position relative to TSS
992 (i.e. negative values represent promoter region whereas positive values represent gene body).
993 **B**, As for A, but for H3K9ac. **C**, As for A, but for H4K5ac.

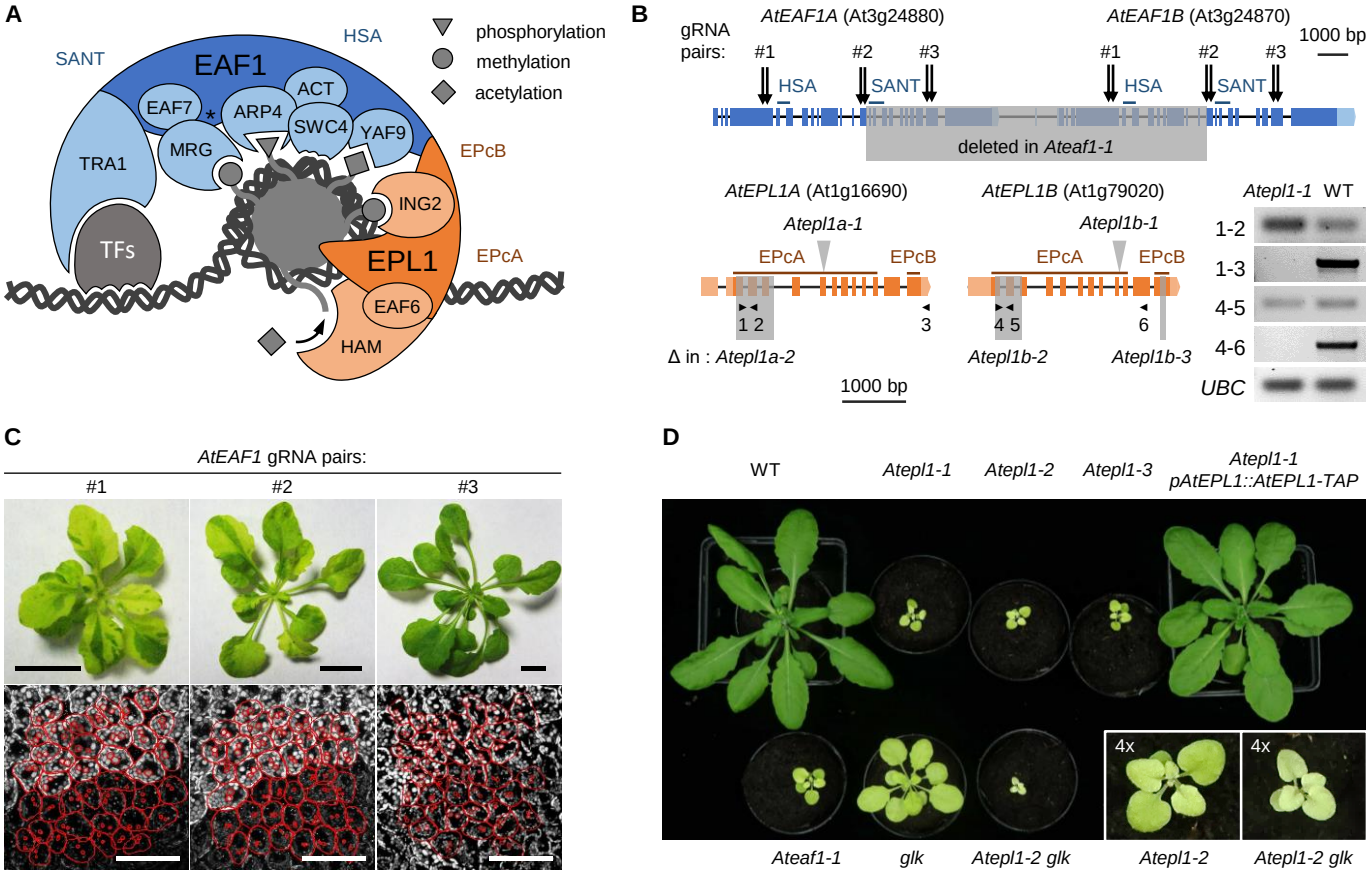

Figure 1. *Ateaf1* and *Atepl1* mutants as tools for genetic dissection of the plant NuA4 complex

A. Schematic overview of the NuA4 complex engaging chromatin. The catalytic module picNuA4 and the regulatory module are colored orange and blue, respectively. The asterisk between EAF7 and ARP4 indicates the lack of an EAF5 homologue in plants. Approximate positions of the crucial protein domains are indicated by the labels outside the shapes representing the subunits.

B. Gene structure diagrams of the *AtEAF1* and *AtEPL1* loci. Target sites for the three double-gRNA constructs (gRNA pairs) used for *AtEAF1* mutagenesis are depicted by arrows. Shaded areas delimit Cas9-gRNA-induced deletions (Δ) characterizing particular alleles. Grey arrowheads indicate T-DNA insertion sites. Small black arrowheads represent primers used for the RT-PCR presented in the panel on the right.

C. Transgenic plants carrying the three different Cas9-gRNA constructs. The scale bar length is 10 mm in all images. Lower panels are confocal images of chlorophyll autofluorescence in the palisade mesophyll cell layer of a leaf, centered on the border regions between green (upper part) and pale green (lower part) sectors. Red outlines delimit selected cells and chloroplasts. The scale bar is 50 µm in all micrographs.

D. 4 week-old WT and mutant plants grown in the same conditions. The insets show 4x magnifications of the same image.

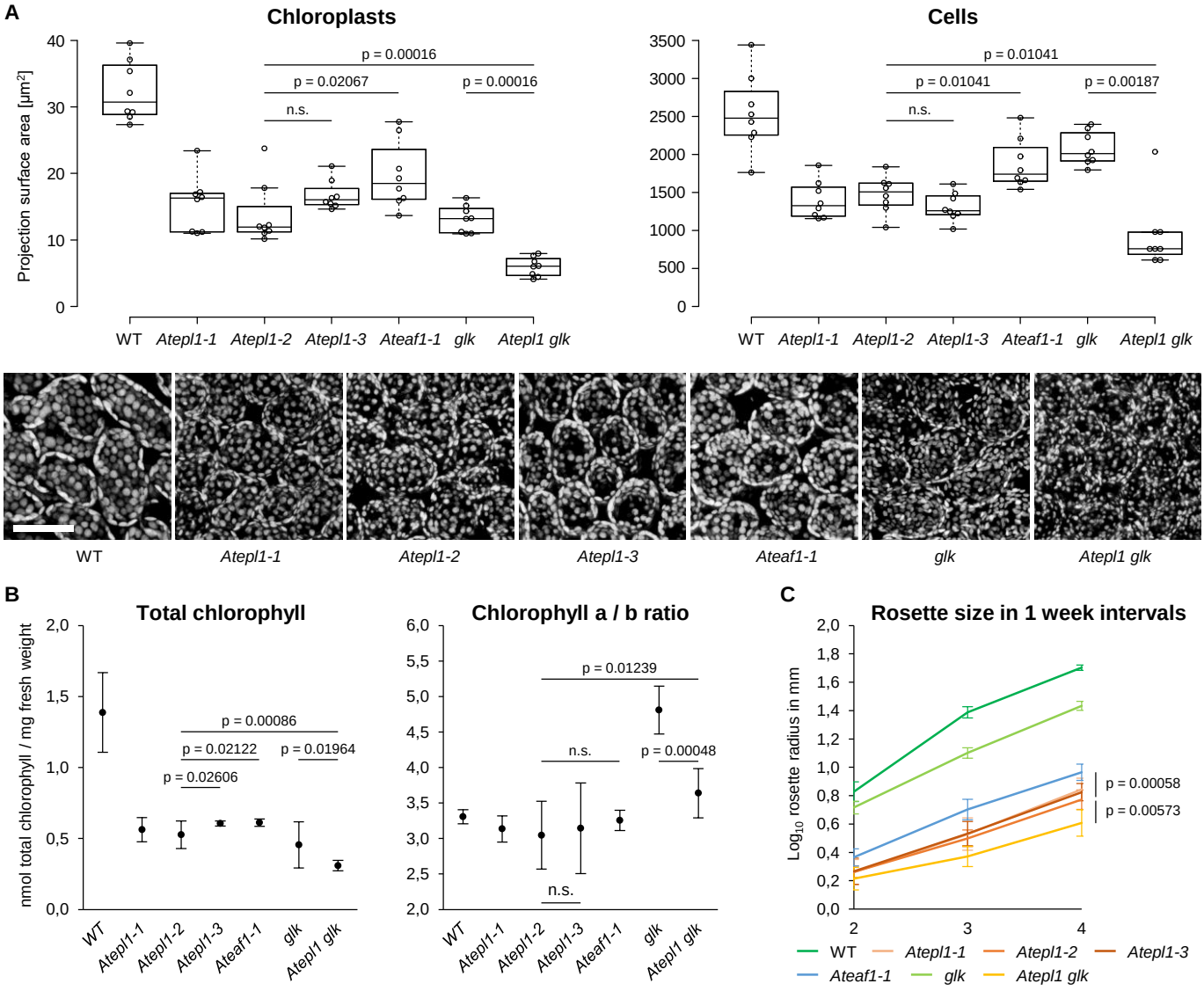

Figure 2. Phenotypic analysis of the NuA4 and GLK mutant lines

A. Quantification of the chloroplast- and cell-size data acquired by microscopic imaging of the palisade mesophyll cell layer. Each circle represents a median surface area of 20 chloroplasts or 9 cells measured in a single biological replicate (a single confocal stack from a separate plant). Statistical significance was determined by two-tailed Mann-Whitney U test. The chlorophyll autofluorescence images below the plots are projections of example stacks used for the measurements. All images are in the same scale. The length of the scale bar is 50 µm.

B. Determination of total chlorophyll content and chlorophyll a / b ratio by spectroscopic analysis of extracted chlorophyll. Dots represent means of 3 biological replicates. The whiskers delimit 95% confidence intervals. Statistical significance was determined by two-tailed t test.

C. Quantification of the growth phenotype of the mutants. The nodes represent the mean rosette radius of 10 or 20 (*Atepl1-2*) plants grown in parallel. The whiskers delimit 95% confidence intervals. P values are given for *Atea1-1* vs *Atepl1-2* (upper) and *Atepl1-2* vs *Atepl1 glk* (lower) comparisons. Statistical significance was determined by two-tailed t test.

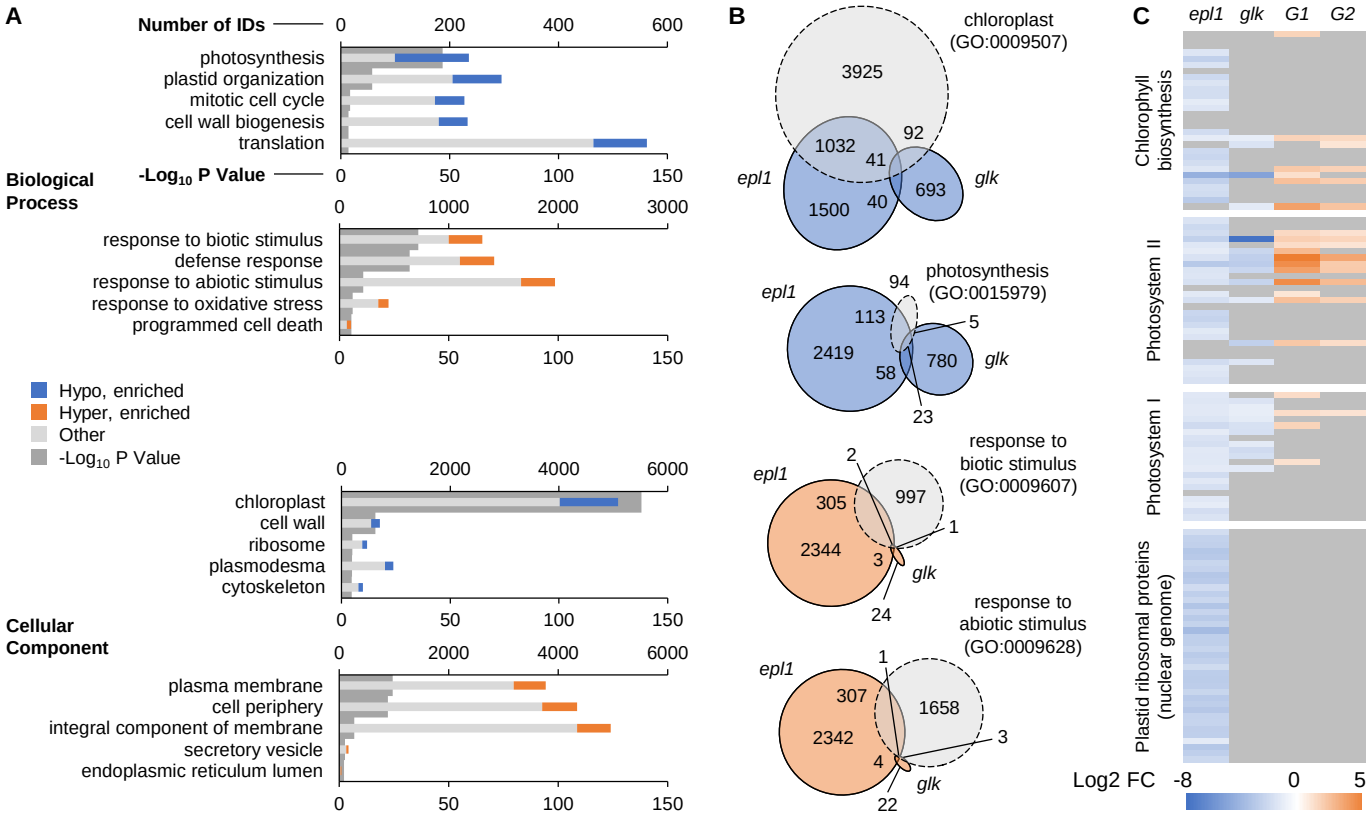

Figure 3. Transcriptomic analysis of the NuA4 and GLK mutants

A. Gene ontology enrichment analysis of the *Atepl1-1* hypo- and hyperactive genes. Five representative GO categories displayed in each graph were selected manually from the lists presented in Supplementary Data 1. Gene enrichment analyses were performed using PANTHER Overrepresentation Test (Supplementary Data 1).

B. Area proportional Venn diagrams illustrating overlaps between genes exhibiting the same direction of expression change in *Atepl1-1* and *glk1* mutants as well as the gene sets representing particular GO categories. All numerical values indicate numbers of genes present in a single sector of the diagram rather than total values for sets.

C. Relative transcript levels of genes encoding four selected groups of chloroplast proteins in *Atepl1-1*, *glk*, *GLK1ox* (*G1*) and *GLK2ox* (*G2*) lines. Expression data for the *glk* mutant and *GLKox* lines come from published works. Grey fields indicate no significant change.

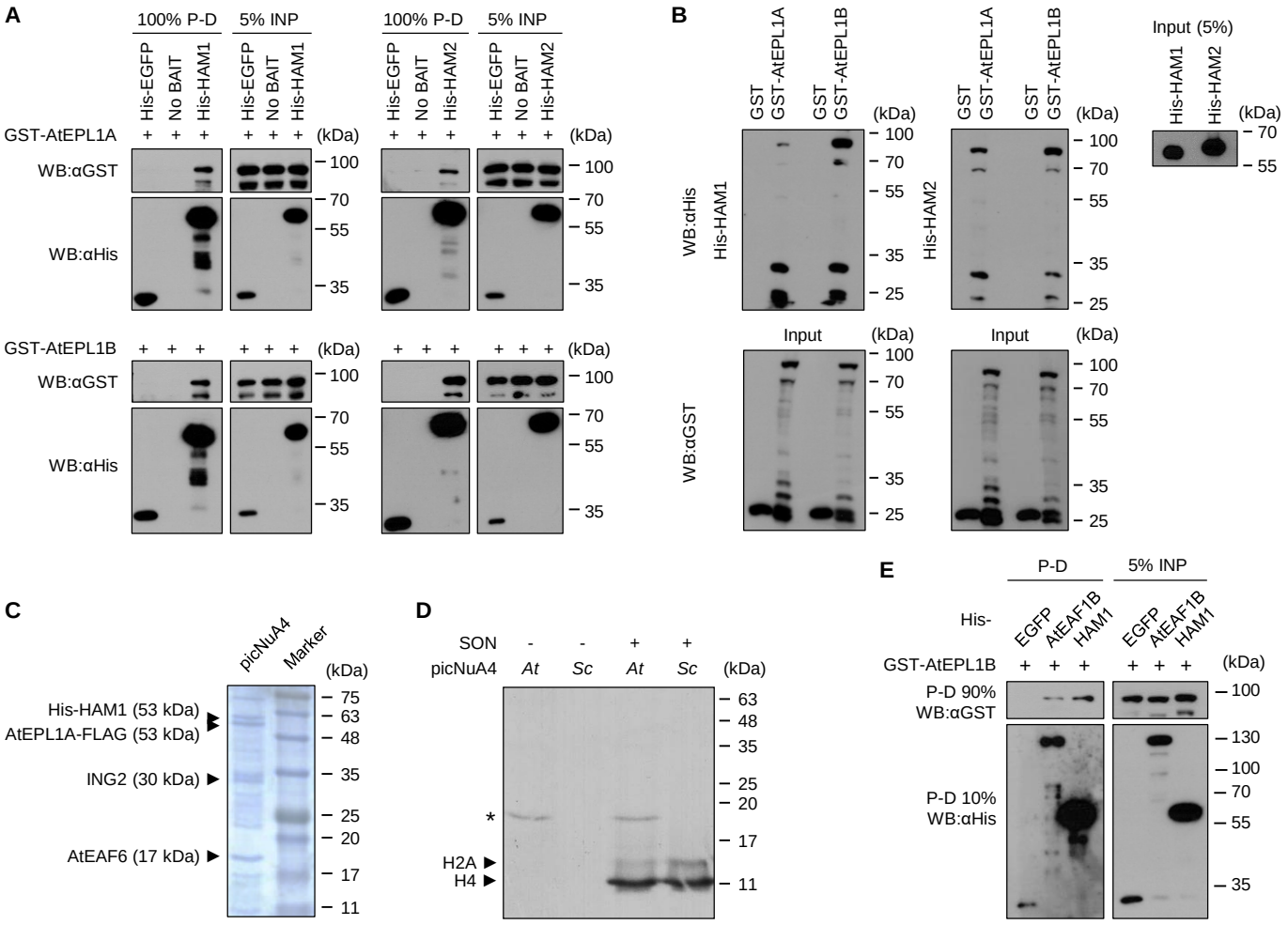

Figure 4. Biochemical characterization of the plant picNuA4

A. Pull-down assay showing interaction between recombinant AtEPL1 and HAM paralogue pairs expressed in bacteria. Pull-down and Input are abbreviated as P-D and INP, respectively.

B. Interactions between AtEPL1s and HAMs tested by Far Western Blot approach. After SDS-PAGE and Western Blot of free GST and GST-AtEPL1A/B, the upper membranes were sequentially incubated with HisHAM1/2 and anti-His antibody whereas the lower membranes were incubated with anti-GST antibody. The lower bands in the upper panels most probably indicate HAM1/2 interaction with partially degraded AtEPL1B.

C. Purification of the recombinant *A. thaliana* picNuA4 from bacteria (left panel, Coomassie staining). 6xHis-tag fused to HAM1 was used for purification on cobalt affinity resin. Numbers in brackets indicate expected molecular weights of the recombinant picNuA4 subunits.

D. In vitro test of HAT activity of the recombinant *A. thaliana* (*At*) picNuA4 towards short oligonucleosomes (SON). Recombinant *S. cerevisiae* (*Sc*) picNuA4 was used as a positive control. Autoacetylation on AtEAF6 is highlighted by an asterisk.

E. Pull-down assay showing the interaction between AtEPL1B and a fragment of AtEAF1B corresponding to AA 430-1322. HAM1 is used for comparison. All proteins were expressed in bacteria as either GST- or 6xHis-fusions.

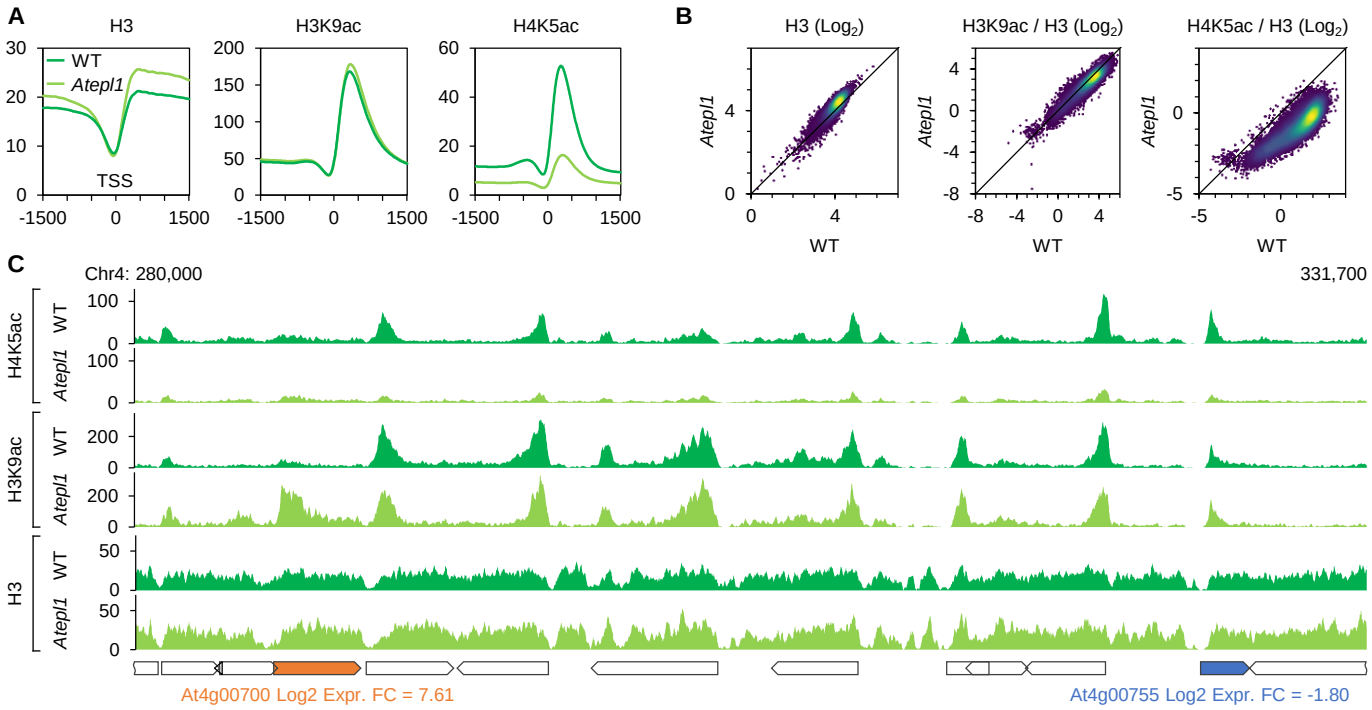

Figure 5. Chromatin landscape of the *Atepl1-2* mutant

A. TSS-centered profiles of spike-in-normalized occupancy of H3, H3K9ac or H4K5ac averaged over all genes expressed in WT Col-0. Vertical axes values are relative. Horizontal axes values represent chromosomal position relative to TSS (i.e. negative values represent promoter region whereas positive values represent gene body).

B. Scatter plots showing differences in H3, H3K9ac or H4K5ac occupancy between *Atepl1-2* and WT. Each dot represents Log_2-transformed ChIP-seq signal averaged over the first 500 bp downstream from TSS of a single gene in WT and in *Atepl1-2*. The number of dots per pixel is color-coded.

C. A fragment of chromosome 4 showing spike-in-normalized H3, H3K9ac or H4K5ac occupancy across several loci. The particular chromosomal location was chosen to illustrate chromatin environment changes coinciding with increased (orange gene) or decreased (blue) transcript levels versus no significant change (white). Vertical axes values are relative.

A

Level 1
Genes hypoactive in *Atepl1*
(Log_2 Expr. FC < -1.5, 1384 genes)

↓

Level 2
Genes that lose H4K5ac in *Atepl1*
(Log_2 H4K5ac FC < -2, 651 genes)

↓

Level 3
Genes that do not lose H3K9ac in *Atepl1*
(Log_2 H3K9ac FC > -0.5, 350 genes)

↓

Level 4
Significantly enriched terms
(Level 3 vs. Level 1)

B

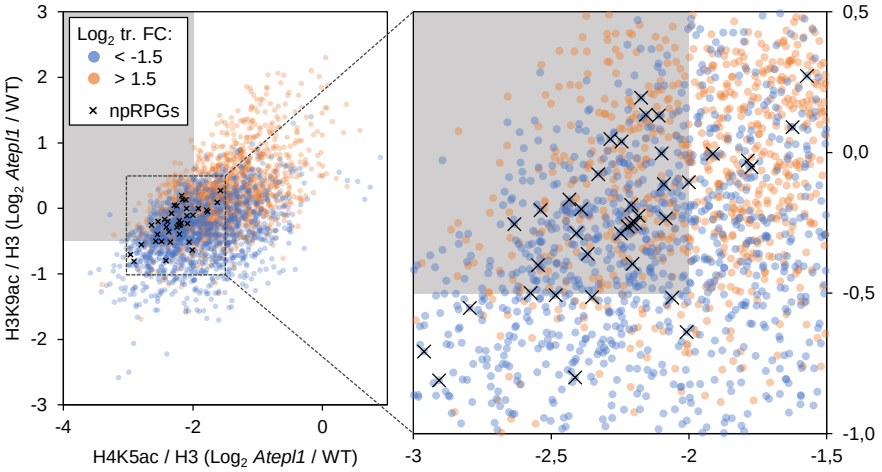

C

Category	Term	Count	%	P Value	FDR	Med. FC	P Value
GT Cellular Component	Chloroplast	214	61.1	7.59E-28	8.63E-25	-2.04	5.80E-01
UP Keywords	Plastid	148	42.3	2.83E-24	3.56E-21	-2.06	8.88E-01
UP Sequence Feature	transit peptide:Chloroplast	74	21.1	3.53E-15	4.75E-12	-2.18	1.65E-01
GT Cellular Component	Chloroplast stroma	83	23.7	4.55E-12	5.17E-09	-2.11	3.27E-01
GT Cellular Component	Chloroplast envelope	70	20.0	1.45E-08	1.65E-05	-2.22	5.87E-02
UP Keywords	Ribosomal protein	26	7.4	2.04E-06	2.58E-03	-2.72	8.32E-05
GT Cellular Component	Plastid	22	6.3	3.53E-06	4.01E-03	-1.83	4.56E-02
GT Cellular Component	Ribosome	26	7.4	4.34E-06	4.93E-03	-2.54	1.11E-03
UP Keywords	Ribonucleoprotein	28	8.0	6.19E-06	7.81E-03	-2.64	9.98E-05
GT Cellular Component	Chloroplast thylakoid membrane	53	15.1	7.17E-06	8.15E-03	-2.03	8.59E-01
GT Biological Process	Translation	26	7.4	1.34E-05	1.89E-02	-2.73	1.61E-05
KEGG Pathway	Ribosome	23	6.6	5.63E-05	5.72E-02	-2.73	1.01E-04
GT Molecular Function	Structural constituent of ribosome	24	6.9	6.86E-05	9.28E-02	-2.73	2.30E-05
All potentialy NuA4-dependent genes		350	100.0	-	-	-1.98	1.01E-02
All genes hypoactive in *Atepl1-1* by more than -1.5 log_2		1384	-	-	-	-2.05	-

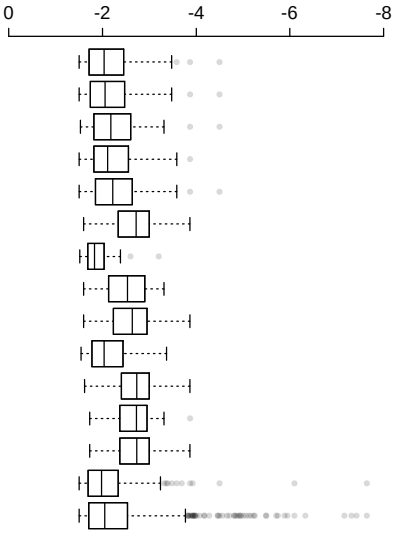

Figure 6. Identification of the potentially NuA4-dependent genes

A. Ideogram of the NuA4-dependency determination process.

B. Scatter plot showing relationships between Log_2-transformed fold-change of the spike-in- and H3-normalized H3K9ac and H4K5ac occupancy and the directionality of the transcript level change. The dashed line delimits the "NuA4-dependent" area of the plot as described in (A).

C. Functional enrichment and relative expression of NuA4-dependent genes. P value for functional enrichment (column 5) is equivalent to EASE score (modified Fisher Exact test, see Methods). P values for the differences between median fold change against all genes hypoactive in *Atepl1-1* (column 8) are results of Mann Whitney U test. GT stands for GO Term.

Table 1. TAP-MS data for AtEPL1B combined with metaanalysis of the previously published AP-MS experiments using NuA4 subunits as baits

	Sc name	At gene	At name	AtARP4	AtARP4	AtSWC4	HAM1	HAM2	AtEPL1A	AtEPL1B	AtYAF9A	AtEPL1B
Complexes				NuA4, SWR1, SWI/SNF, INO80	NuA4, SWR1, SWI/SNF, INO80	NuA4, SWR1	NuA4, PEAT	NuA4, PEAT	NuA4	NuA4	NuA4, SWR1	**NuA4**
Model				cell culture	cell culture	cell culture	seedlings	seedlings	seedlings	seedlings	seedlings	**seedlings**
Background				PSB-D line	T87 line	T87 line	WT	WT	WT	WT	*Atyaf9a-1*	***Atepl1-1***
Promoter				CaMV35S	UBQ10	UBQ10	native	native	native	native	CaMV35S	**native**
Tag				GS TAP tag	Strep	Strep	Myc	Myc	Flag	Flag	GH TAP tag	**GS TAP tag**
Reference				Vercruyssen	Bieluszewski	Bieluszewski	Tan	Tan	Tan	Tan	Crevillen	**This work**
NuA4 subunits	**ARP4**	AT1G18450	AtARP4	+	+	+	+	+	+	+	+	**2 / 1.78**
		AT1G73910	AtARP4A		+	+						
	SWC4	AT2G47210	AtSWC4		+	+	+		+	+	+	**2 / 1.63**
	YAF9	AT5G45600	AtYAF9A	+	+	+	+	+	+	+	+	**2 / 1.42**
		AT2G18000	AtYAF9B			+				+		
	EAF1	AT3G24880	AtEAF1A		+	+	+	+	+	+	+	**2 / 0.42**
		AT3G24870	AtEAF1B		+	+	+					**2 / 0.43**
	TRA1	AT2G17930	AtTRA1A						+	+		**2 / 0.37**
		AT4G36080	AtTRA1B			+		+	+	+		**2 / 0.44**
	ESA1	AT5G64610	HAM1		+	+	+		+	+	+	**2 / 0.95**
		AT5G09740	HAM2			+		+				**1 / 0.16**
	EPL1	AT1G16690	AtEPL1A			+	+		+			
		AT1G79020	AtEPL1B		+	+		+		+		**2 / 2.22**
	YNG2	AT1G54390	ING2		+	+	+		+	+		**2 / 1.50**
	EAF6	AT4G14385	AtEAF6		+	+	+		+	+		**2 / 1.96**
	EAF3	AT4G37280	MRG1			+	+					**2 / 0.29**
		AT1G02740	MRG2									
	EAF5	-	-									
	EAF7	AT1G26470	AtEAF7			+						
Additional AtEPL1B interactors detected here		AT2G31810	AHASS1									**2 / 0.21**
		AT3G07810	AOG2				+					**2 / 0.18**
		AT3G60110	BRD6			+	+					**2 / 0.06**
		AT1G48520	GATB									**1 / 0.06**
		AT1G26570	UGD1									**1 / 0.04**
Number of additional bait-specific hits				2	454	1104	331	280	96	241	114	**0**

Numbers in the rightmost column indicate number of biological replicates (out of two) in which the protein was detected as well as its relative abundance in the final eluate analyzed by mass spectrometry (Normalized Spectral Abundance Factor, NSAF, see Methods).